Research Square

Preprints are preliminary reports that have not undergone peer review.
They should not be considered conclusive, used to inform clinical practice,
or referenced by the media as validated information.

Refined Optimal and Modified-Homotopy Perturbation Method for Direct Solution of Incompressible Navier-Stokes Equations with Pressure Correction

Tapas Roy
Vidyasagar University
Dilip Kumar Maiti
d_iitkgp@yahoo.com

Vidyasagar University
Palash Mondal
Vidyasagar University

Research Article

Keywords: Computational Methods, Series solution, Non-Newtonian flow, Incompressible flow

Posted Date: August 31st, 2026

DOI: https://doi.org/10.21203/rs.3.rs-10656307/v1

License: This work is licensed under a Creative Commons Attribution 4.0 International License.
Read Full License

Additional Declarations: No competing interests reported.

Refined Optimal and Modified-Homotopy Perturbation Method for Direct Solution of Incompressible Navier-Stokes Equations with Pressure Correction

Tapas Roy[a], Dilip Kumar Maiti[a,*], Palash Mondal[a,b]

[a]*Department of Applied Mathematics, Vidyasagar University, Midnapur-721102, WB, India.*

[b]*Department of Mathematics, Subarnarekha Mahavidyalaya, Gopiballavpur, Jhargram-721506, India*

Abstract

Motivation and Method Development: Direct semi-analytical treatment of the full two-dimensional (2D) incompressible Navier–Stokes equations (INSE) with simultaneous determination of velocity and pressure fields, remains a challenging problem in fluid mechanics, particularly for Newtonian and non-Newtonian internal flows. To address this challenge without simplifying the governing PDEs or reducing them to ODEs, a Refined Optimal and Modified Homotopy Perturbation Method (ROM-HPM) is developed. The framework provides systematic guidelines for selecting auxiliary linear operators and constructing initial approximations for PDEs. Arbitrary functions arising in the auxiliary solutions are represented by polynomials with unknown coefficients determined directly from the prescribed initial and boundary conditions. A pressure-correction algorithm is incorporated to overcome the inability of the standard OM-HPM formulation to adequately treat pressure-coupled incompressible flows. Necessary and sufficient conditions for convergence are established, together with truncation error, stability, and computational complexity analyses.

Application to Newtonian and Non-Newtonian Microchannel Flows: ROM-HPM is applied directly to the full 2D INSE governing Newtonian and non-Newtonian flows in microchannels with non-unifrom injection-suction and slip boundary conditions under both prescribed and unknown pressure fields. The resulting semi-analytical velocity and pressure solutions are validated against available exact solutions and established computational fluid dynamics (CFD) results. Beyond reproducing benchmark flow fields, the method captures the transient development of coherent flow structures and resolves their evolution from elongated and partially developed vortices to fully developed vortical patterns.

Flow Physics, Validation and Computational Performance: Comparisons between continuous and discrete implementations of ROM-HPM and conventional CFD demonstrate strong agreement in velocity, pressure, and associated flow structures while revealing advantages in computational efficiency, solution accuracy, convergence behaviour, and extension of the computational domain. The results demonstrate that ROM-HPM provides a direct semi-analytical framework for resolving pressure velocity coupling in the full 2D INSE while preserving the underlying flow physics, offering an alternative computational route for investigating complex incompressible internal flows.

Keywords: Computational Methods, Series solution, Non-Newtonian flow, Incompressible flow.

*Corresponding author

E-mail addresses: $roytapas0096@gmail.com$ (T. Roy), $d_iitkgp@yahoo.com$ (D.K. Maiti*)

1. Introduction

Despite being formulated in the 19th century, obtaining a complete analytical solution of the full Navier–Stokes (N–S) equations without simplifications remains an open problem in fluid dynamics [1], owing to their inherent nonlinearity, pressure dependence, and complex boundary conditions. In particular, for three-dimensional (3D) flows, this challenge is recognized as one of the seven Millennium Prize Problems established by the Clay Mathematics Institute in 2000 [1].

The difficulty of solving the N-S equations analytically has led to the development of computational fluid dynamics (CFD) [2] as a primary tool for simulation and analysis. However, conventional CFD methods [2] such as finite difference (FDM), finite volume (FVM), and finite element methods (FEM) are widely used but face several challenges, such as high computational cost, grid resolution issues, numerical errors, long computation time, and stability concerns. Moreover, CFD approaches lack general expressions for the solutions. Instead, semi-analytical methods can provide broader insights across domains through generalized solutions. Nevertheless, to date, the exact analytical solution of the complete incompressible Navier-Stokes equations (INSE) without simplifications has not been found. Existing analytical or semi-analytical studies [3–9] typically address reduced forms obtained through traveling-wave, self-similarity, or other transformations. Note that, these equations are central to analyzed flows of fluids such as air, water, blood, and plasma, and have wide applications in weather prediction [10], engineering [11, 12], and medical applications [13, 14]. Solving the full N–S equations directly, without reducing them to simplified forms, is crucial for accurately capturing nonlinear behaviors such as vortex dynamics, boundary-layer separation, and complex transport phenomena [15]. In addition, analyzing non-Newtonian flows [14, 16] is more challenging than Newtonian fluids [17] due to their highly nonlinear and coupled nature, and research on non-Newtonian fluids is still limited. Recent works have explored models like Casson, power-law, and viscoelastic fluids, often applying similarity transformations to obtain analytical or numerical solutions [7–9, 14].

Pressure is a fundamental physical quantity that significantly influences fluid behavior, whether at rest or in motion. In incompressible flows, unlike velocity, pressure lacks an explicit equation and must be determined indirectly. Various analytical and numerical approaches exist for this purpose. For example, Majee et al. [14] solved the full INSE for MHD blood flow in a wavy artery using the vorticity–stream function formulation, where pressure is eliminated and later recovered from the velocity field. In primitive variable approaches [2, 16, 18, 19], pressure is computed using the Semi-Implicit Method for Pressure-Linked Equations (SIMPLE) algorithm [20]. In SIMPLE, pressure is calculated using the pressure correction formula, and this correction is obtained by solving the Poisson equation, which is derived by utilizing the continuity equation to ensure incompressibility (1a). Others [21, 22] employ the Pressure Poisson Equation (PPE), derived from the momentum and continuity equations, though its use is limited by difficulties in specifying boundary or initial conditions for pressure is remaining a key challenge in solving INSE.

Semi-analytical methods become popular because they bypass discretizations, thereby avoiding associated numerical errors, and offer flexibility along with closed-form or near closed-form analytical solutions to otherwise intractable nonlinear problems. However, most of the previous authors including [6–9, 23–25] have neglected the pressure gradient term due to the transformations (either through stream functions, vorticity formulations, or traveling wave). While this simplification reduces the mathematical complexity and enables analytical tractability, it can yield physically inconsistent results, particularly in incompressible flows, where the pressure field must be determined from the coupled continuity and momentum equations. Thus, although semi-analytical and numerical methods are well-suited for general classes of PDEs, they may fall short when applied to

incompressible flow problems, which inherently require accurate treatment of both the velocity and pressure fields.

Homotopy Analysis Method (HAM) [4, 5, 8, 24, 26–28, 52] and Homotopy Perturbation Method (HPM) [29] are two widely used semi-analytical techniques for obtaining analytical solutions of nonlinear differential equations [30]. However, it should be noted that, in most fluid dynamical problems, HAM and HPM are typically employed to the simplified form (in ODE) of the INSE [6, 8, 24, 25]. As per Liao [4, 6, 7], the main pillar of HAM are (i) auxiliary linear operator (A.L.O) ($\mathcal{L}$), (ii) initial guess (u_0), (iii) artificial auxiliary parameter ($\hbar$), and (iv) artificial auxiliary function ($H(x)$). These artificial auxiliary parameter or functions are known as controlling parameters for convergence. Now, without last two factors, HAM reduces to HPM. Therefore, HPM is special case of HAM, when artificial parameters $H(x) = 1$ and $\hbar = -1$ and have same $\mathcal{L}$ [31, 32]. Despite the success of the HPM, HAM and related semi-analytical techniques, there were several methodological limitations remains long-standing opened [25, 37], particularly the absence of rigorous mathematical methodology to choose $\mathcal{L}$ and its optimal form, basis functions, and u_0 [25, 26, 37]. As a consequence, HAM and HPM provides locally convergent series solution in most of the cases [6, 32].

A review of existing literature [30, 38, 39] reveals that authors often select u_0 either by setting $t = 0$ in an exact solution or using analytical results obtained by previous researchers, or, from the solution of very simplified form of the original equation, and thereafter they have chosen the $\mathcal{L}$ [6, 8, 25]. These u_0 are chosen to be as close as possible to the exact solution, which introduces subjectivity into the method. Baxter et al. [30] explored the application of homotopy-based methods to solve Cahn-Hilliard type initial value problems, which are relatively simpler, involving a single partial differential equation (PDE). However, in their analysis, the convergence control parameter $\hbar$ was found to be approximately zero, which contradicts the core principle of HAM ($\hbar \neq 0$). Baxter et al. [30] further observed that: "While a number of nonlinear ODEs and nonlinear PDEs reducible to ODEs via traveling waves, self-similarity, or other transformations have been solved using homotopy analysis, solving general PDEs with arbitrary initial data remains rare due to methodological challenges. These results point to a need for future development in solving strongly nonlinear PDEs through techniques such as HAM and optimal HAM". Therefore, the applicability of HPM, HAM and its variants in fluid dynamical problems remains questionable.

Therefore, the major shortcomings of semi-analytical methods, including HAM and HPM, in fluid mechanics can be summarized as follows:

- *No rigorous framework*: Lack of universal mathematical guidelines for selecting the auxiliary linear operator (A.L.O) $\mathcal{L}$ and initial guess u_0. This issue remains an open challenge, as repeatedly noted by Liao [6, 25, 26] and more recently by Liu and Liu [37].

- *Lacks of globally convergent solutions:* Both HAM and HPM fails to provide the globally convergent series solution, especially for the initial value problems (IVPs). $\hbar$ and $H(x)$ of HAM can only accelerate rate of convergence but not the domain of convergence [32–34].

- *Unrealistic pressure treatment:* There is no established method for handling the continuity and pressure fields without simplifications for INSE. Forming PPE [21, 22] encounter boundary related challenges.

- *No direct solutions:* As per Baxter et al. [30], not all fluid dynamical problems can be reduced to ODEs through traveling-wave, self-similar, or other transformations. Moreover, as of now,

there is no efficient semi-analytical method by which one can obtain the direct solution of the complete INSE.

We have addressed the above first two methodological limitations in our earlier works [31, 32, 34] through the development of an advanced semi-analytical approach, namely the Optimal and Modified Homotopy Perturbation Method (OM-HPM), which is free from the artificial parameters $\hbar$ and $H(x)$ of HAM, and is similar to HPM only in the sense of the homotopy equation and the embedding parameter. However, the key distinction from conventional HPM is that OM-HPM deals with a general A.L.O $\mathcal{L}$ and initial guess u_0, which contain some unknown auxiliary roots (refer section-2.1.2). That is, in OM-HPM the convergence-controlling parameters are inherently present in the form of unknown auxiliary roots. By minimizing the residual error, OM-HPM determines these optimal roots and consequently an optimal $\mathcal{L}$. Through both theoretical and numerical experiments on several complex nonlinear problems, including IVPs and singular BVPs, we validated Liao's claim [6, 7, 26] that "a perfect choice of $\mathcal{L}$ is more important than $\hbar$ and $H(x)$ of HAM." We proved that the optimal auxiliary roots are self-sufficient for ensuring convergence and hence global convergence, while artificial parameters $\hbar$ and $H(x)$ have no significant contribution in enhancing the domain of convergence or reducing homotopy truncation, except for a few limited accelerations in the rate of convergence [31, 32, 34]. Therefore, we refrain from the use of artificial parameters $\hbar$ and $H(x)$ of HAM. More recently, we extended this concept beyond the HAM framework to the Variational Iteration Method (VIM) and proposed a refined version, termed Refined VIM (R-VIM) [33]. Here also both theoretically and numerically we demonstrated that, similar to homotopy-based methods (HAM/HPM), the proper selection of the linear operator plays a more decisive role in ensuring convergence than the use of any artificial convergence-control parameters.

Although Liao [26] has attempted to construct an optimal A.L.O by introducing an arbitrary constant in the coefficients in linear operator and minimizing the residual while solving Gelfand equation. However, Liao could not succeed. In particular, for a second-order PDEs proved that the second order linear operator is useless since the solution diverges. Consequently, a fourth and sixth-order operators were introduced, which contradicts the fundamental principle of structural consistency in the HAM, despite its flexibility. Moreover, Liao [26] himself conclude that "*it is a pity that many things about the HAM are still unclear now for nonlinear differential equations in general. For example, how to find the best or the optimal A.L.O among an infinite number of possible ones? Can we give some rigorous mathematical proofs in general?* ". In contrast, we construct a universal A.L.O of the same order as the governing equation, with coefficients based on auxiliary roots. By minimizing residuals, we obtain a dynamic optimal A.L.O, showing that such computation is feasible and efficient, contrary to earlier claims [25, 26, 40]. However, some challenges for PDEs still remain unresolved.

To address the aforementioned open challenges in the field of semi-analytical methods for fluid mechanics, the present study aims to extend and refine OM-HPM for the direct solution of PDEs, including the full INSE, without reducing them to ODEs or any simplifying assumptions. To solve the full 2D INSE including both the pressure gradient and the continuity equation the standard OM-HPM framework alone is inadequate due to the absence of a separate governing equation for pressure. Therefore, to ensure that the computed solutions satisfy the fundamental physical laws (conservation of mass and momentum), an additional algorithm is essential within the OM-HPM framework to handle the pressure gradient and continuity constraint. Thereby we named as ROM-HPM, R stands refined. Therefore, our aim of this study are:

1. Develop a general mathematical framework for selecting A.L.O and suitable initial approximations when applying OM-HPM to partial differential equations, including the full form of the

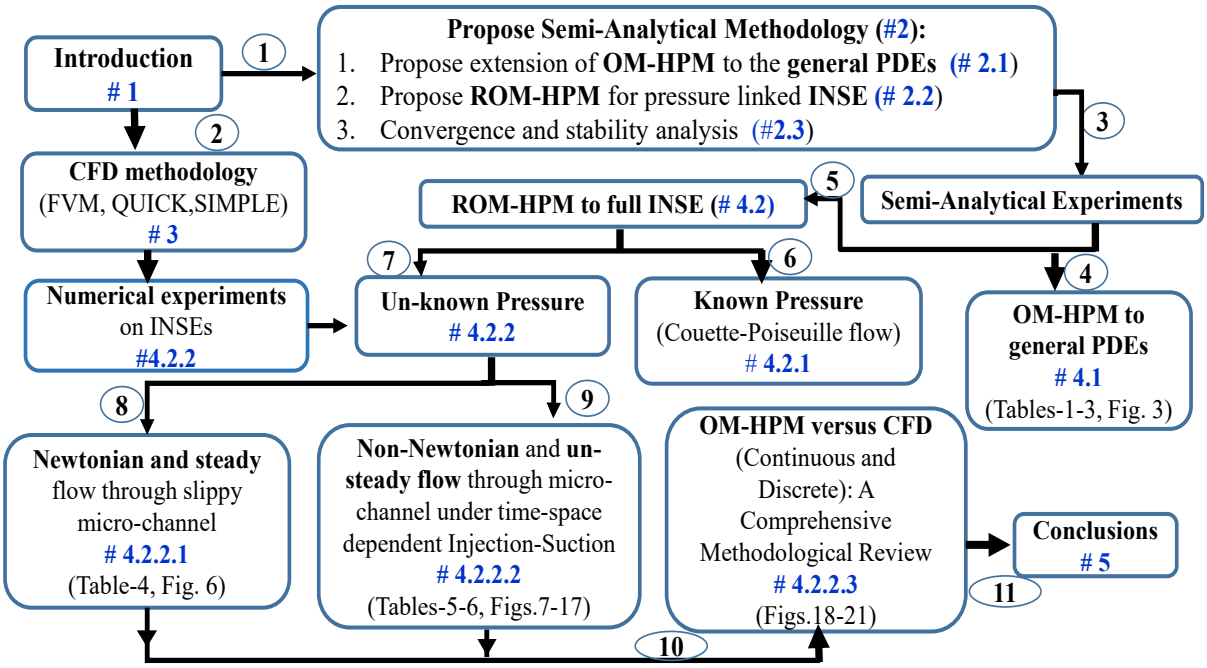


Fig. 1: Schematic overview of the state-of-the-art of this study. The numbers within the circles for each arrow help to understand the flow of reading the entire manuscript at a glance. Additionally, sub-section numbers are also written within each box.

2D INSE.

2. Propose an additional algorithm to be embedded within the OM-HPM framework (ROM-HPM) to accurately compute the pressure field and utilise continuity equation in incompressible flows governed.
3. Establish necessary and sufficient conditions for convergence of our scheme, and quantify the associated truncation error, scaling complexity, resulting stability characteristic.
4. Conduct a semi-analytical experiment on approximating arbitrary functions (arises in the initial approximation) within the auxiliary solution framework of PDE using polynomials with unknown coefficients, determined through initial and boundary conditions.
5. Perform semi-analytical experiments of OM-HPM on general PDEs and then ROM-HPM on the complete 2D INSE, both Newtonian and non-Newtonian for cases with both known and unknown pressure fields.
6. Validate and compare the results obtained via ROM-HPM with the exact solution (when available) and established CFD methods (Staggered grid, Finite Volume Method (FVM), Quadratic Upstream Interpolation for Convective Kinematics (QUICK) and SIMPLE).
7. Investigate the capability of ROM-HPM to capture unsteady flow features in the N-S equations.
8. Analyze the physical formation and evolution of coherent structures, such as elongated, partially developed, and fully developed vortices in a micro-channel flow (without any obstacle against the flow) under time varying injection-suction mechanisms, and distinguish these from classical Karman vortices based on their dynamic characteristics and formation processes.
9. Systematically compare our ROM-HPM with CFD techniques by analyzing their similarities, differences, advantages, and limitations, and demonstrate the superior performance of ROM-HPM, particularly in its continuous form, with respect to a physically realistic solution and computational efficiency.

The comprehensive state of art of this work is presented in Fig.1 from where one can easily grasp the overall framework of the study and gain an initial understanding at a glance.

2. Propose Semi-Analytical Methodology:

In our earlier research [31], we applied our OM-HPM [31, 34, 36] to the following incompressible Navier-Stokes equations (INSE) for a porous channel with orthogonally moving walls [8]

$$\frac{\partial u}{\partial x}+\frac{\partial v}{\partial y}=0 \tag{1a}$$

$$\frac{\partial u}{\partial t}+u\frac{\partial u}{\partial x}+v\frac{\partial u}{\partial y}+\frac{\partial p}{\partial x}-\frac{1}{Re}\left(\frac{\partial^2 u}{\partial x^2}+\frac{\partial^2 u}{\partial y^2}\right)=0, \tag{1b}$$

$$\frac{\partial v}{\partial t}+u\frac{\partial v}{\partial x}+v\frac{\partial v}{\partial y}+\frac{\partial p}{\partial y}-\frac{1}{Re}\left(\frac{\partial^2 v}{\partial x^2}+\frac{\partial^2 v}{\partial y^2}\right)=0, \tag{1c}$$

where Re is the Reynolds number. These INSE were transformed into ODEs using similarity transformations. While doing so, the pressure gradient terms were eliminated. As a sequel to our previous study [31], our aim here is to upgrade the OM-HPM (section 2.1) so that it can be directly applied to PDEs, including the INSE (1a)–(1c), along with an additional algorithm (section 2.2) to handle the pressure gradient terms and the continuity equation (1a) under incompressibility constraints. Therefore, without simplification, this extension of our OM-HPM, to be named as refined OM-HPM (ROM-HPM) is intended to preserve the key flow features and physical properties.

2.1. OM-HPM framework for solving PDEs

Let us initially discuss the OM-HPM algorithm for a system of general nonlinear PDEs of order n with two unknowns $u(x,y,t)$ and $v(x,y,t)$, defined as

$$\mathcal{N}_1\left[u(x,y,t),v(x,y,t)\right]=0,\quad \mathcal{N}_2\left[u(x,y,t),v(x,y,t)\right]=0,\quad x,y,t\in D \tag{2}$$

subject to initial condition (I.C) and boundary conditions (B.C)

$$\mathcal{I}_1\left(u,\frac{\partial u}{\partial t}\right)=0,\quad \mathcal{I}_2\left(v,\frac{\partial v}{\partial t}\right)=0,\ t\in\Gamma_1,\ \text{and} \tag{3a}$$

$$\mathcal{B}_1\left(u,\frac{\partial u}{\partial x}\right)=0,\ x\in\Gamma_2,\ \mathcal{B}_2\left(v,\frac{\partial v}{\partial y}\right)=0,\ y\in\Gamma_3 \tag{3b}$$

where $\mathcal{N}_1$ and $\mathcal{N}_2$: general nonlinear partial differential operator of order n, $\mathcal{I}_1$ and $\mathcal{I}_1$: I.C operators, and $\mathcal{B}_1$ and $\mathcal{B}_2$: B.C operators, potentially representing Dirichlet, Neumann, or Robin-type conditions, Γ_1: time domain, Γ_2 and Γ_3: spatial boundaries along x and y, respectively. As per the computational requirement of homotopy based methods including OM-HPM, we defined the following three sub-sections:

2.1.1. Formulation of Homotopy Equations

For the solution of the general PDE described in Eqs. (2)-(3) using a homotopy-based method, it is necessary to construct homotopy equations that continuously deform the selected auxiliary linear operator (A.L.O) into the original nonlinear problem. Accordingly, the zero-th order and higher (mth) order homotopy equations are defined as follows:

Zero-th order Homotopy equations: The zero-th order homotopy equations for the two unknowns u and v of the nonlinear system (2) are , respectively,

$$(1-q)\mathcal{L}_1\left[\phi - u_0(x,y,t,\lambda_1,...,\lambda_n)\right] + q\,\mathcal{N}_1[\phi,\theta] = 0 \tag{4a}$$
$$(1-q)\mathcal{L}_2\left[\theta - v_0(x,y,t,r_1,...,r_n)\right] + q\,\mathcal{N}_2[\phi,\theta] = 0 \tag{4b}$$

where $\mathcal{L}_1$, $\mathcal{L}_2$: the auxiliary linear operators (A.L.Os), $(\lambda_1, \lambda_2, ..., \lambda_n)$ and $(r_1, r_2, ..., r_n)$ are auxiliary roots of $\mathcal{L}_1$ and $\mathcal{L}_2$, respectively (as defined in section-2.1.2). u_0 and v_0 are initial guess for unknowns u and v, respectively, which satisfies I.C (3a) and B.C, and (3b) are the solution of $\mathcal{L}_1[u] = 0$ and $\mathcal{L}_2[v] = 0$, respectively. $\phi = \phi(x,y,t,\lambda_1,...,\lambda_n,r_1,...,r_n,q)$ and $\theta = \theta(x,y,t,\lambda_1,...,\lambda_n,r_1,...,r_n,q)$ are intermediate variables for u and v, respectively, which are series solution of the homotopy equations (4a) and (4b), in terms of the embedding parameter $q \in [0,1]$, as defined

$$\phi = u_0(x,y,t,\lambda_1,...,\lambda_n) + \sum_{m=1}^{+\infty} u_m(x,y,t,\lambda_1,...,\lambda_n,r_1,...,r_n)q^m, \tag{5a}$$
$$\theta = v_0(x,y,t,r_1,...,r_n) + \sum_{m=1}^{+\infty} v_m(x,y,t,\lambda_1,...,\lambda_n,r_1,...,r_n)q^m \tag{5b}$$

Here, $u_m(x,y,t,\lambda_1,...,\lambda_n,r_1,...,r_n)$ and $v_m(x,y,t,\lambda_1,...,\lambda_n,r_1,...,r_n)$ denotes the m^{th} order approximations of the OM-HPM. Finally, in an iterative sense, the finite (m th order) approximate solution of the original nonlinear equation (2) can be computed by putting $q = 1$ in (5a)-(5b) as

$$u \approx \phi(x,y,t,\lambda_1,...,\lambda_n,r_1,...,r_n,1) = \sum_{i=0}^{m} u_i(x,y,t,\lambda_1,...,\lambda_n,r_1,...,r_n) \tag{6a}$$
$$v \approx \theta(x,y,t,\lambda_1,...,\lambda_n,r_1,...,r_n,1) = \sum_{i=0}^{m} v_i(x,y,t,\lambda_1,...,\lambda_n,r_1,...,r_n), \tag{6b}$$

which contain some unknown auxiliary roots (λ_i, r_i, $i = 1,2,\ldots,n$) of $\mathcal{L}_1$ and $\mathcal{L}_2$. The optimal values of these λ_i and r_i are to be determined by minimizing the residual error (ref. Section-2.1.3), which leads to the optimal forms of $\mathcal{L}_1$ and $\mathcal{L}_2$. For details of the entire deformation process with respect to $q \in [0,1]$, readers are referred to the HAM [6, 7] and OM-HPM [31, 32, 34].

Higher (m-th) order Homotopy equations (iterative formula): To derive the general mth order iterative scheme, let us define the vectors corresponding to u and v, respectively, as

$$\vec{u}_m = \{u_0, u_1, u_2, ..., u_m\}, \quad \vec{v}_m = \{v_0, v_1, v_2, ..., v_m\}. \tag{7}$$

Now, substituting the series (5a) and (5b) into the equations (4a) and (4b), respectively, and equating the like-power of q, we can derive a higher order homotopy equation. Accordingly we derive the m-th order homotopy equation as

$$\mathcal{L}_1[u_m - \chi_m\, u_{m-1}] + R_{u_{m-1}}[\vec{u}_{m-1}, \vec{v}_{m-1}] = 0,\ m \geq 1 \tag{8a}$$
$$\mathcal{L}_2[v_m - \chi_m\, v_{m-1}] + R_{v_{m-1}}[\vec{u}_{m-1}, \vec{v}_{m-1}] = 0,\ m \geq 1 \tag{8b}$$

where

$$R_{u_{m-1}}[\vec{u}_{m-1}, \vec{v}_{m-1}] = \frac{1}{(m-1)!}\frac{\partial^{m-1}}{\partial q^{m-1}}\mathcal{N}_1[\phi,\theta]\Big|_{q=0}, \tag{9a}$$

$$R_{v_{m-1}}\left[\vec{u}_{m-1},\vec{v}_{m-1}\right]=\frac{1}{(m-1)!}\frac{\partial^{m-1}}{\partial q^{m-1}}\mathcal{N}_2\left[\phi,\theta\right]\Big|_{q=0} \tag{9b}$$

and

$$\chi_m=\begin{cases}0, & m\leq 1;\\ 1, & m>1.\end{cases} \tag{10}$$

As results of equations (8a) and (8b), we have a special solutions as

$$u_m^*=\chi_m u_{m-1}-\mathcal{L}_1^{-1}R_{u_{m-1}}\left[\vec{u}_{m-1},\vec{v}_{m-1}\right],\ v_m^*=\chi_m v_{m-1}-\mathcal{L}_2^{-1}R_{v_{m-1}}\left[\vec{u}_{m-1},\vec{v}_{m-1}\right] \tag{11}$$

where the last term $(R_{u_{m-1}},R_{v_{m-1}})$ is known as homotopy correction term, also knows as homotopy residual. Consequently, the iterative scheme for the general solution takes the form

$$u_m=u_m^*+u_{C.F},\ v_m=v_m^*+v_{C.F},m\geq 1 \tag{12}$$

subjected to the I.C (3a) and B.C (3b), where $u_{C.F}$ and $v_{C.F}$ are the solution of $\mathcal{L}_1[u]=0$ and $\mathcal{L}_2[v]=0$, respectively, and known as complimentary solutions that contains arbitrary constants. The form of $u_{C.F}$ and $v_{C.F}$ are noted in Eq.(15) as presented in section-2.1.2.

2.1.2. General rule for selections of auxiliary linear operators (A.L.O) and initial approximations for general PDEs

In order to start the iteration for the homotopy equations (4a)-(4b), it is essential to define an appropriate auxiliary linear operator $\mathcal{L}_1[u]$ and $\mathcal{L}_2[v]$, which serves as the backbone of the OM-HPM formulation. The choice of these $\mathcal{L}_1$ and $\mathcal{L}_2$ are not arbitrary, rather, it is designed to (i) admit analytically tractable solutions, and (ii) provide sufficient flexibility to control the convergence of the perturbation series. Building on our earlier studies on ODEs [31–34], the A.L.O is constructed as a homogeneous linear operator with constant coefficients parameterized by a set of auxiliary roots. In the present framework, this concept is extended to the PDE setting by constructing analogous operators in terms of selected pairs of independent variables, say (x,y). For u variable, $\mathcal{L}_1[u]$ is chosen as a homogeneous linear partial differential operator with constant coefficients as

$$\mathcal{L}_1\left[u(x,y,t,\lambda_1,\ldots,\lambda_n)\right]=\frac{\partial^n u}{\partial x^n}+a_{n-1}\frac{\partial^n u}{\partial x^{n-1}\partial y}+a_{n-2}\frac{\partial^n u}{\partial x^{n-2}\partial y^2}+\cdots+a_0\frac{\partial^n u}{\partial y^n} \tag{13}$$

where the constant co-efficient $a_{n-k},k=1,2,\ldots n$ are parameterized in terms of a set of auxiliary roots $\{\lambda_i\}_{i=1}^n$ of $\mathcal{L}_1[u]=0$, defined in our previous studies [31–34]. As an example, for $n=2$ and $n=3$, $\mathcal{L}_1[u]$ takes the form, respectively,

$$\mathcal{L}_1\left[u(x,y,t,\lambda_1,\lambda_2)\right]=\frac{\partial^2 u}{\partial x^2}-(\lambda_1+\lambda_2)\frac{\partial^2 u}{\partial x\partial y}+\lambda_1\lambda_2\frac{\partial^2 u}{\partial y^2},\quad \text{and} \tag{14a}$$

$$\mathcal{L}_1\left[u\right]=\frac{\partial^3 u}{\partial x^3}-(\lambda_1+\lambda_2+\lambda_3)\frac{\partial^3 u}{\partial x^2\partial y}+(\lambda_1\lambda_2+\lambda_2\lambda_3+\lambda_1\lambda_3)\frac{\partial^3 u}{\partial x\partial y^2}+\lambda_1\lambda_2\lambda_3\frac{\partial^3 u}{\partial y^3}. \tag{14b}$$

This representation permits the operator $\mathcal{L}_1[u]$ to be constructed directly from its characteristic structure, such that its null space is spanned by functions of the form $f(y+\lambda_i x,t)$. Consequently, the specification of the auxiliary roots uniquely determines the operator $\mathcal{L}_1[u]$. These roots play a central role, analogous to the convergence-control parameter $\hbar$ in the homotopy analysis method (HAM).

The selection of the independent variable pair is problem-dependent. That is, operator (13) is a template and not indeed for all PDEs. While (x,y) is adopted here, alternative pairs such as (x,t),

(y, t), or their permutations may be employed to align the operator with the dominant physical processes (e.g., convection or temporal evolution) in the governing equations. In the literature [38, 41], it is seen that a time dependent problem can be solved using time independent pairs.

Although the general solution of $\mathcal{L}_1[u] = 0$ contains arbitrary functions [50] and is therefore non-unique, its structure is crucial for constructing the initial approximation u_0. Depending on the nature of the auxiliary roots (real distinct, repeated, or complex conjugate), different functional forms arise. For instance, in the case of real and distinct roots, the general solution takes the form

$$u_0(x, y, t, \lambda_1, \ldots, \lambda_n) = \sum_{i=1}^{n} f_i(y + \lambda_i x, t) \tag{15}$$

where f_i's, $i = 1, 2, .., n$ are arbitrary functions, which are to be computed using the given I.C (3a) and B.C (3b). In the present study we consider this case of real and distinct roots. Besides this choices of u_0 for real-distinct (15), one can consider real-equal or complex conjugate roots, whose explicit forms can be found in [50].

To determine the arbitrary functions f_i, we adopt either of the following two approaches: (i) an exact approach, or (ii) an approximate approach. In the exact approach, the given initial and/or boundary conditions (IC/BC) are directly applied, and efforts are made to extract the explicit functional forms of f_i. However, in many practical situations, this approach becomes infeasible due to either insufficient IC/BC or the resulting system of equations for f_i being unsolvable (see example-4.1.1, 4.1.2, 4.2.1, 4.2.2.1, 4.2.2.2). In such cases, the approximate approach is employed, wherein the arbitrary functions f_i are assumed to be polynomial functions with undetermined coefficients. These coefficients are subsequently evaluated using the available IC/BC (see example-4.1.1, 4.1.2, 4.2.1, 4.2.2.1, 4.2.2.2). It is important to emphasize that the auxiliary roots are not constrained a priori. Their primary role is to act as tuning parameters that influence the convergence behaviour of the OM-HPM series solution, rather than the final physical solution itself. Indeed, our earlier studies [31–34] indicate that the solution is largely insensitive to the specific choice of these roots, although the rate of convergence and computational complexity may vary marginally. In particular, increasing the number of auxiliary parameters enhances flexibility but leads to higher algebraic complexity in the deformation equations. Therefore, a balance must be maintained between convergence control and computational efficiency.

A similar construction applies to the auxiliary operator $\mathcal{L}_2$ for the homotopy equations (4b), with a distinct set of roots to ensure linear independence, i.e., $\mathcal{L}_1 \neq \mathcal{L}_2$.

2.1.3. **Residual minimization and dynamic-optimal linear operators**

In OM-HPM, at least one root among λ_i's and/or r_i's, $i = 1, 2, ..., n$ must be assumed unknown, then the optimal $\mathcal{L}_1$ and $\mathcal{L}_2$, as well as the optimal convergence solution at a particular order (m) are obtained by computing the optimum value of these unknowns based on minimization of the square residuals of $\mathcal{N}_1$ and $\mathcal{N}_2$ together simultaneously. The exact square residual for $\mathcal{N}_1$ is defined as:

$$\Delta_{u_m}(\lambda_i, r_i) = \int_{\Gamma_1}\int_{\Gamma_2}\int_{\Gamma_3} \left(\mathcal{N}_1 \left[\sum_{k=0}^{m} u_k(x, y, t, \lambda_i, r_i), \sum_{k=0}^{m} v_k(x, y, t, \lambda_i, r_i) \right] \right)^2 dx\, dy\, dt \tag{16}$$

This was proposed by Yabushita et al. [53]. Unfortunately, this method consumes huge CPU time. In order to decrease CPU time and inline with Liao [7] we discretise the above square residual based on numerical integration method (Simpson's $\frac{1}{3}$ rule [31]) as

$$\Delta_{u_m}(\lambda_i, r_i) \approx$$
$$\frac{h}{3}\sum_{j=1}^{\frac{\sigma}{2}}\sum_{k=1}^{\frac{\sigma}{2}}\sum_{l=1}^{\frac{\sigma}{2}}\left\{\left(\mathcal{N}_1\left[\sum_{s=0}^{m}u_s(x_{2j-2},y_{2k-2},t_{2l-2},\lambda_i,r_i),\sum_{s=0}^{m}v_s(x_{2j-2},y_{2k-2},t_{2l-2},\lambda_i,r_i)\right]\right)^2\right.$$
$$+4\left(\mathcal{N}_1\left[\sum_{s=0}^{m}u_s(x_{2j-2},y_{2k-2},t_{2l-2},\lambda_i,r_i),\sum_{s=0}^{m}v_s(x_{2j-2},y_{2k-2},t_{2l-2},\lambda_i,r_i)\right]\right)^2 \tag{17}$$
$$\left.+\left(\mathcal{N}_1\left[\sum_{s=0}^{m}u_s(x_{2j-2},y_{2k-2},t_{2l-2},\lambda_i,r_i),\sum_{s=0}^{m}v_s(x_{2j-2},y_{2k-2},t_{2l-2},\lambda_i,r_i)\right]\right)^2\right\}$$

where $u_s\,(x, y, t, \lambda_i, r_i)$ is the s-th order truncated perturbation solution, $h = \frac{b-a}{\sigma}$, σ =even number. It should be noted that our Newton-Cotes formula is superior compared to the weighted residuals (least-squares, Collocation and Galerkin) methods discussed in [7, 8, 25], as it offers higher-order accuracy and can capture the curvature of the entire function rather than only its mean value. Similarly, one can define the square residual $\Delta_{v_m}(\lambda_i, r_i)$ based on $\mathcal{N}_2$. Then, the optimal auxiliary roots (λ_i^*, r_i^*) are to be compute using the following condition [8, 33]

$$\Delta_m(\lambda_i^*, r_i^*) = Min\left\{\Delta_{u_m}(\lambda_i, r_i), \Delta_{v_m}(\lambda_i, r_i) = 0\right\} \tag{18}$$

where Δ_m is the minimum value of above formula (18) corresponding to (λ_i^*, r_i^*). After substituting the optimal values of auxiliary roots (λ_i^*, r_i^*) at a particular m we have the optimal $\mathcal{L}_1$ and $\mathcal{L}_2$. Also the series solutions (6) becomes optimal solution after substituting optimal values of (λ_i^*, r_i^*). Needless to mention that our $\mathcal{L}$ changes as order m changes, since the value of (λ_i^*, r_i^*) changes as m increases. Therefore, it is dynamic overall. It is clear that during the optimization process, a system of nonlinear algebraic equations involving (λ_i, r_i), $i = 1, 2, .., n$ are to be solved subject to the constraint $\Delta_{v_m}(\lambda_i, r_i) = 0$, where the number of equations involved in the optimization process (18) increases with the number of unknowns (λ_i, r_i). Consequently, a larger number of unknowns results in higher computational cost (longer CPU time).Therefore, introducing more unknowns increases the overall scaling complexity in two phases: first, during the iterative solution process, and second, during the residual minimization process.

2.2. Embedding additional algorithm for pressure gradient into OM-HPM framework for solving INSE (1) directly: Renaming to ROM-HPM

To solve the complete 2D INSE (1a)-(1c), which include the pressure gradient and continuity equation, the aforesaid OM-HPM (ref. section-2.1) alone is not sufficient. This is because there are three dependent variables, namely u, v and p, and applying OM-HPM (section-2.1) to Eqs.(1b) and (1c) we could get velocities u and v, however, there is no explicit equation for the pressure p as well as Eq.(1a) is left to utilize. Therefore, an additional algorithm needs to be embedded within the OM-HPM framework to handle the pressure gradient term and incorporate the continuity equation, ensuring that the computed solutions adhere to the fundamental physical laws: conservation of mass and momentum. To distinguish this approach from the earlier OM-HPM developed for ODEs and, more recently, for PDEs in Section-2.1, the present modification where OM-HPM is extended to incorporate pressure-correction computation for INSE (1) naturally leads us to designate it as the refined OM-HPM (ROM-HPM). Now the complete computational algorithm of ROM-HPM to compute u, v and p together by solving the system (1) is noted step wise.

Step-1: *Utilization of continuity equation:* Substitute the continuity equation (1a) into the remaining momentum equations (1b) and (1c), and we have the revised governing equations as:

$$\mathcal{N}_1(u,v,p) = \frac{\partial u}{\partial t} - u\frac{\partial v}{\partial y} + v\frac{\partial u}{\partial y} + \frac{\partial p}{\partial x} - \frac{1}{Re}\left(\frac{\partial^2 u}{\partial y^2} - \frac{\partial^2 v}{\partial x\,\partial y}\right) = 0 \tag{19a}$$

$$\mathcal{N}_2(u,v,p) = \frac{\partial v}{\partial t} + u\frac{\partial v}{\partial x} - v\frac{\partial u}{\partial x} + \frac{\partial p}{\partial y} - \frac{1}{Re}\left(\frac{\partial^2 v}{\partial x^2} - \frac{\partial^2 u}{\partial x\,\partial y}\right) = 0 \tag{19b}$$

Step-2: *Choice of initial velocity and pressure:* As outlined in section-2.1.2, the initial approximations $u_0(x,y,t)$ and $v_0(x,y,t)$ are computed from $\mathcal{L}_1[u] = 0$ and $\mathcal{L}_2[v] = 0$, respectively, with given IC and BC. However, pressure does not have an explicit governing equation, nor does it possess prescribed IC and/or BC. Therefore, inspired by the SIMPLE algorithm [18, 20], we choose $p_0(x,y,t)$ hypothetically.

Step-3: *Derivation of correctional terms:* The initial velocities ($u_0(x,y,t)$, $v_0(x,y,t)$) and pressure ($p_0(x,y,t)$) are to be corrected. Applying OM-HPM (Section 2.1) to the revised momentum equations (19a) and (19b) we compute m-th order correctional velocities u_m and v_m (12), respectively. Onece the mth order velocity correction u_m and v_m are computed using Eqs. (11)–(12) along with the previous $(m-1)$th-order terms, we need to determine the corrections for the pressure gradients $\frac{\partial p_m}{\partial x}$ and $\frac{\partial p_m}{\partial y}$ to execute the next iteration. As per the homotopy frame, we use the following homotopy residual of Eqs. (19a) and (19b) at the m the order

$$\begin{aligned} R_{u_{m-1}}(\vec{u}_{m-1},\vec{v}_{m-1}) =& \frac{\partial u_{m-1}}{\partial t} - \sum_{k=0}^{m-1} u_k \frac{\partial v_{m-k-1}}{\partial y} + \sum_{k=0}^{m-1} v_k \frac{\partial u_{m-k-1}}{\partial y} + \frac{\partial p_{m-1}}{\partial x} \\ & - \frac{1}{Re}\left(\frac{\partial^2 u_{m-1}}{\partial y^2} - \frac{\partial^2 v_{m-1}}{\partial x\,\partial y}\right),\ m \geq 1 \end{aligned} \tag{20a}$$

$$\begin{aligned} R_{v_{m-1}}(\vec{u}_{m-1},\vec{v}_{m-1}) =& \frac{\partial v_{m-1}}{\partial t} + \sum_{k=0}^{m-1} u_k \frac{\partial v_{m-k-1}}{\partial x} - \sum_{k=0}^{m-1} v_k \frac{\partial u_{m-k-1}}{\partial x} + \frac{\partial p_{m-1}}{\partial y} \\ & - \frac{1}{Re}\left(\frac{\partial^2 v_{m-1}}{\partial x^2} - \frac{\partial^2 u_{m-1}}{\partial x\,\partial y}\right),\ m \geq 1 \end{aligned} \tag{20b}$$

In order to compute corrected $\frac{\partial p_m}{\partial x}$ and $\frac{\partial p_m}{\partial y}$ and hence to determine pressure correction formula, we assumed that $R_{u_{m-1}}(\vec{u}_{m-1},\vec{v}_{m-1}) = 0$ and $R_{v_{m-1}}(\vec{u}_{m-1},\vec{v}_{m-1}) = 0$ and hence from (20a)-(20b) for $m \geq 1$ we can derive the following formulas:

$$\frac{\partial p_m}{\partial x} = \frac{\partial p_{m-1}}{\partial x} - R_{u_{m-1}}(\vec{u}_{m-1},\vec{v}_{m-1}),\ m \geq 1 \tag{21a}$$

$$\frac{\partial p_m}{\partial y} = \frac{\partial p_{m-1}}{\partial y} - R_{v_{m-1}}(\vec{u}_{m-1},\vec{v}_{m-1}),\ m \geq 1 \tag{21b}$$

These are the computational formula for corrected pressure gradients at each ROM-HPM iterations. It may be noted that in SIMPLE algorithm [18, 20], the velocity is updated iteratively using pressure correction calculated from the Poisson equation, derived from the continuity condition to enforce the incompressibility constraint. Whereas here we correct the pressure gradients (Eqs.(21a)-(21b)) iteratively using the homotopy residuals of velocities (20a)-(20b), which are in terms of all previous correctional velocity components: $\{u_0, u_1, u_2, ..., u_{m-1}\}$ and $\{v_0, v_1, v_2, ..., v_{m-1}\}$. Therefore, these formulas are analogous to a multi-step method for solving initial value problems numerically. Thus, this approach is expected to give more accurate results. Moreover, the homotopy

residuals $R_{u_{m-1}}$ and $R_{v_{m-1}}$ (see (20a)-(20b)) inherently contain the continuity equations (ref. step-1). It is worth noting that our approach circumvents the boundary-condition difficulties typically associated with the pressure-Poisson equation [21, 22].

Step-4: *Solution as a finite series form:* Collect all homotopy corrections and write the final solution at the mth order as a finite series (6a) of the form

$$u\left(x,y,t,\lambda_i,r_i\right) \approx \sum_{k=0}^{m} u_k(x,y,t,\lambda_i,r_i),\ v\left(x,y,t,\lambda_i,r_i\right) \approx \sum_{k=0}^{m} v_k(x,y,t,\lambda_i,r_i),$$
$$\frac{\partial p\left(x,y,t,\lambda_i,r_i\right)}{\partial x} \approx \sum_{k=0}^{m} \frac{\partial p_k\left(x,y,t,\lambda_i,r_i\right)}{\partial x} \text{ and } \frac{\partial p\left(x,y,t,\lambda_i,r_i\right)}{\partial y} \approx \sum_{k=0}^{m} \frac{\partial p_k\left(x,y,t,\lambda_i,r_i\right)}{\partial y} \quad (22)$$

Note that these approximate velocity and pressure gradient expressions contain the unknown auxiliary roots λ_i and r_i, where $i = 1, 2$. As discussed in section-2.1.3, these unknown auxiliary roots are determined by minimizing the square residuals based on $\mathcal{N}_1(u,v)$ and $\mathcal{N}_2(u,v)$ defined in Eq. (17). Needless to mention, these square residuals depend on the above velocity as well as the pressure correctional terms.

2.3. Convergence, computational efficiency, and stability analysis of the OM-HPM and hence ROM-HPM

It has been theoretically proved in our previous study [33, 34] that the contraction ($\|u_{m+1}\| < \|u_m\|, \forall m > M$, i.e., $\|u_m\| \to 0$ as $m \to \infty$) holds if the following condition is satisfied:

$$0 \leq \mu = \mathcal{L}^{-1}\{1\} < \frac{1}{|\hbar|\ \|H(x)\|}. \quad (23)$$

where $\hbar$ and $H(x)$ are the artificial auxiliary parameter and function, respectively, of HAM [6, 7, 25, 26]. Note that, this is the necessary condition for the convergence of homotopy based methods including HPM, HAM, optimal HAM and OM-HPM. For the linear operators containing only higher-order terms (i.e., all auxiliary roots $\lambda_i = 0$ in Eq.(13)), which are usually considered by previous authors [26, 38, 41] in homotopy-based methods except OM-HPM, it has been proved in our previous study [33, 34] that these contemporary methods fail to satisfy this necessary condition for convergence (23) beyond a certain range of the domain. Hence it may be deduced that homotopy-based methods with this kind of linear operator provide only locally convergent series solutions. This can be confirmed from the observation of Gorder (Chapter-4 of [6]) where it is reported that the solutions generated by such $\mathcal{L}$ whose basis functions are polynomials, usually converge only locally. It is worth noting that with the linear operator as defined in Eq.(13) (a homogeneous linear operator with auxiliary roots as coefficients [31–34]) and for a suitable negative value of λ_i, our OM-HPM satisfy the necessary condition $(0 \leq \mu < 1)$ for convergence in the whole domain. In ODE [31, 32, 34], OM-HPM generates expression with exponential decay basis, beginning from u_0.

Here in the context of PDEs, u_0 of the OM-HPM (15) may not necessarily contain an exponential basis, since arbitrary functions involved in u_0 (Eq.(15)) are to be computed in an approximated approach (Eqs. (46), (49), (51), (54), (60)). It is worthy to note that the general inverse operator contains exponential terms. It propagates exponential terms at each iteration, and hence the final series solution contains an exponential basis (ref. Eqs.(33), (61a), (61b), (61c) similar to ODEs). As an example, for the general PDEs of order (n=1) we have $\mu = \frac{e^{\lambda_1(x-x_0)}-1}{\lambda_1}$ and for the INSE (1a)-(1c) (n=2) we have $\mu = \frac{e^{\lambda_1(x-x_0)}-1}{\lambda_1(\lambda_1-\lambda_2)} + \frac{e^{r_1(x-x_0)}-1}{r_1(\lambda_1-\lambda_2)}$. Then, (a) for $\lambda_1 > 0$,, or/and $\lambda_2 > 0$, μ

grows unboundedly and fails contraction condition (23) beyond some x, regardless of $\hbar$ or $H(x)$; (b) for $\lambda_1 < 0$ and and $\lambda_2 < 0$, contraction may hold for all $x > 0$, provided λ_1 and λ_2 are not too small. For $\lambda_1 < 0$ and $\lambda_2 < 0$, the homotopy higher-order terms will contain decaying exponential base functions, forcing them to satisfy the aforesaid contraction condition. It is to be numerically demonstrated in Tables- 4-6 that optimal value of controlling parameter eventually attain negative value.

After satisfying the necessary condition, one should verify the sufficient condition to ensure the convergence, which is discussed as follows:

Theorem: [6, 33, 40]

Let $\Delta_m(\lambda_1, ..., \lambda_n, r_1, ..., r_n)$ be the residual error of the computed OM-HPM series solution $\phi_m(x, y, t, \lambda_1, ..., \lambda_n, r_1, ..., r_n, 1)$ at the m-th order approximation corresponding to $\mathcal{N}[u(x, y, t)] = 0$. Then, the sufficient condition for the convergence of the series $\phi_m(x, y, t, \lambda_1, ..., \lambda_n, r_1, ..., r_n, 1)$ to the exact solution $u(x, y, t)$ is that for any $\epsilon > 0$

$$\|\Delta_m(\lambda_1, \lambda_2, ..., \lambda_n, r_1, ..., r_n)\| < \epsilon, \ \forall m \geq M \in \mathbb{N}, \ \forall x, y, t > 0 \tag{24}$$

That is, $\Delta_m \to 0$ as $m \to \infty$. Now for a system of nonlinear equation (either (2) or (19)) at which we have the equivalent quantity here as Δ_m defined in Eq.(18). Therefore, residuals Δ_{u_m} and Δ_{v_m} eventually satisfy the above sufficient condition at sufficiently large m. Moreover, while calculating the optimal values (λ_i^*, r_i^*) that satisfy condition (18), inherently provides negative values for (λ_i^*, r_i^*) ([31–33], Tables-1- 5). Therefore, the solutions of OM-HPM satisfy the above necessary and sufficient conditions for convergence over the whole domain. Needless to mention that ROM-HPM is nothing but the OM-HPM with an additional algorithm for pressure gradient calculation of INSE, hence the solution of ROM-HPM also satisfy the above necessary and sufficient condition (ref. Tables- 4-6).

Additionally, for more robustness of our method ROM-HPM to the INSE we would like to further verify whether the obtained solutions (u, v) satisfy the continuity equation (1a), and the computed pressure gradients $\frac{\partial p}{\partial x}$ and $\frac{\partial p}{\partial y}$ satisfy Euler's compatibility condition:

$$(i) \ \frac{\partial u}{\partial x} + \frac{\partial v}{\partial y} = \delta, \quad \text{and } (ii) \ \frac{\partial}{\partial y}\left(\frac{\partial p}{\partial x}\right) - \frac{\partial}{\partial x}\left(\frac{\partial p}{\partial y}\right) = \delta. \tag{25}$$

If the condition is not met within the specified tolerance, say $\delta = 10^{-6}$, proceed to higher-order approximations and continue iterating until the desired accuracy is achieved (ref. Tables-4-6).

It is plausible that semi-analytical methods, including OM-HPM, inherently avoid many numerical errors (such as discretization errors due to truncation, grid-resolution issues, round-off errors, and the need for a finite computational domain) and are therefore generally more stable than conventional numerical techniques. However, contemporary semi-analytical approaches such as HPM, HAM, and their variants often suffer from truncation errors, particularly at lower orders of approximation, because they typically yield finite Taylor series expansions [25, 26] and rely on weighted residual approximations for determining parameters [6]. Moreover, these methods suffer from the choice of suitable linear operator (Chapter-4, [6]). In contrast, OM-HPM [31, 32, 34] produces exponentially decaying base functions, which effectively take care of truncation errors and enables convergence at significantly lower orders of approximation. Consequently, OM-HPM is expected to exhibit superior stability compared to the above semi-analytical methods.

Gorder (Chapter 4, [6]) observed that the stability characteristics of HAM depend strongly on the choice of the linear operator and the convergence-control parameter. Computational efficiency

(measured through rapid convergence with fewer iterations) likewise depends on an appropriate choice of $\mathcal{L}$. A suitable selection of the A.L.O causes the optimal convergence-control parameter to stabilize at a nearly constant value, and the residual error (Δ_m) diminishes rapidly as iteration count increases. This condition is sufficient for ensuring stability, and OM-HPM inherently satisfies it. Our previous studies [31–34] have already demonstrated, both theoretically and numerically (Theorems-2 and 3, [33]) that the error decreases monotonically, the controlling parameter stabilizes, and the dynamic $\mathcal{L}$ approaches to an optimal form with increasing iterations. The same behavior is to be confirmed in the present analysis (Tables-1, 2, and 5). Therefore, following the criteria outlined by Gorder (Chapter-4, [6]), OM-HPM/ROM-HPM exhibits no possibility of poor stability; rather, it consistently ensures high stability. Moreover, OM-HPM and ROM-HPM are computationally efficient.

2.4. Flowchart of OM-HPM for PDE and ROM-HPM for INSE

For better understanding, we summarize the entire process (sec.2.1-sec.2.4) of ROM-HPM for solving the INSE in Fig.2, where we clearly distinguish between the basic mechanism, the main computational steps, and the post-processing phase. When the pressure is explicitly absent from the governing equations and hence it becomes the general PDEs, then ROM-HPM reduces to OM-HPM. One can use the same flowchart for OM-HPM except pressure correction step (step-3).

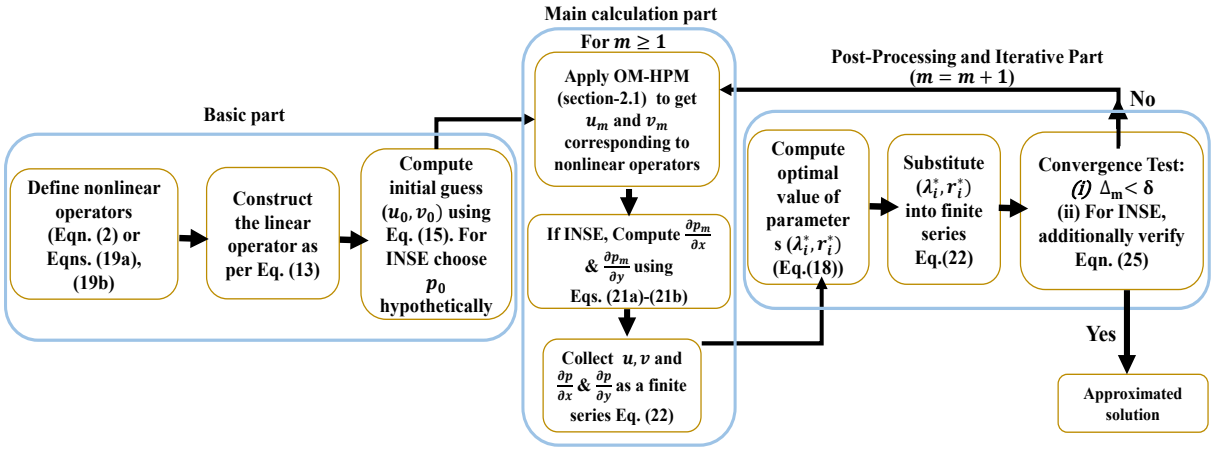


Fig. 2: Flowchart of the proposed ROM-HPM for INSE. The diagram delineates the algorithmic steps: base formulation, core computations, and post-processing stages.

3. Numerical CFD Methodology

A uniform grid is applied along the y-direction, while a non-uniform grid with an initial size Of 0.01 is used along the x-direction, gradually increasing from the channel entrance. The numerical code used in our previous studies [16–19, 49] from our previous work are utilized here. Several comparisons were made to validate our numerical code. Also grid independence study were performed and it is reported that variations in grid size affect the velocity only at the third decimal place for a non-dimensional length of 100 (Ref. [51]). In our latest study [49], We also calculated grid convergence index (GCI) based on three grids (finer, medium and coarse) and the results indicate that the numerical solution is essentially insensitive to grid refinement. Moreover, the relative difference between the coarse and medium grids is comparatively larger, whereas the difference between the medium and fine grids is small, indicating that further grid refinement has a negligible

influence on the solution. Therefore, the 350×120 grid is adopted for all subsequent simulations, as it provides an appropriate balance between accuracy and computational efficiency.

Furthermore, to ensure global conservation and numerical accuracy, detailed diagnostics based on the root mean-square (RMS) of mass and momentum are presented. Numerical convergence is ensured by requiring that the global mean-square residuals of mass and momentum fall below 10^{-4} at each time iteration. The Grid Convergence Index (GCI) analysis, validation of the numerical code, and evaluation of the root-mean-square (RMS) residuals together provide strong evidence of the accuracy and reliability of the present numerical approach. Accordingly, the numerical results obtained from the present code are considered sufficiently accurate, and the findings presented in Section-4.2.2 are well supported.

4. Applicability of the proposed methods (OM-HPM and ROM-HPM) and their validation

We divide this experimental section into two subsections. In the first subsection we testify our OM-HPM on the general PDEs (except INSE), while in the second subsection we apply our ROM-HPM on the pressure-linked complete INSE with known and unknown pressure gradient for Newtonian and non-Newtonian flows in a open microchannels (i.e., without outlet). The second subsection presents our main contribution, where we directly solve the pressure-linked INSE using the proposed ROM-HPM without resorting to traveling waves, self-similarity, vorticity transformation, or other simplifications. We also validate our semi-analytical solutions with those obtained by CFD techniques (staggered grid, FVM, QUICK, and SIMPLE).

4.1. OM-HPM to general PDEs:

Initially we testify our method (OM-HPM) on two general PDEs:

Example-4.1.1: First, we considered the two dimensional (2D) Gelfand equation from Liao [26]:

$$\Delta u + \lambda e^{u} = 0, \quad u\,(x, \pm 1) = 0,\ u\,(\pm 1, y) = 0 \tag{26}$$

While solving this equations (26), Liao [26] considered the A.L.O as

$$\mathcal{L} = \frac{c_2}{x\ y}\frac{\partial^2 u}{\partial x\ \partial y} + c_4 \frac{\partial^4 u}{\partial x^2\ \partial y^2} \tag{27}$$

which is a fourth-order linear homogeneous PDE with variable coefficients. Liao [26] have shown that, although the Gelfand equation involves a linear operator (the Laplacian operator), it cannot be taken as an A.L.O., since the solution does not satisfy the boundary condition at x = 1. Furthermore, it is demonstrated there that when $c_4 = 0$, the second-order linear operator for a second-order problem (26) is ineffective, as it fails to yield a convergent series solution. In contrast, when $c_2 = 0$, the fourth-order linear operator proves to be effective, achieving a residual error on the order of 10^{-4} at the 20th-order approximation. Finally, it has been concluded there that a second-order nonlinear PDE (such as the Gelfand equation) can be transformed into infinitely many fourth-order (in 2D) or sixth-order (in 3D) linear PDEs. In essence, the emphasis is on the flexibility in selecting the A.L.O., often through a trial-and-error approach. Therefore, a key open question remains: *how can one determine the best or optimal auxiliary linear operator from the infinitely many possible choices?* To address this open question, we employ our recently developed advanced semi-analytical method, OM-HPM to this problem and find the optimal A.L.O as per the flowchart outlined in Fig.2 for OM-HPM, we follow the following seven sequential steps:

i. **Choice of nonlinear operator $\mathcal{N}$:** From (26) we have

$$\mathcal{N}[u] = \frac{\partial^2 u}{\partial x^2} + \frac{\partial^2 u}{\partial y^2} + \lambda e^u \tag{28}$$

ii. **General choice of A.L.O ($\mathcal{L}$):** Since the given problem (26) is a second-order ($n = 2$) PDEs with the spatial variables as x, y, the general A.L.O takes the form exactly as defined in (14a).

iii. **Choice of initial approximation $u_0(x, y)$:** Solving $\mathcal{L}_1 [u(x, y)] = 0$ we compute $u_0(x)$ as of the form

$$u_0(x, y, \lambda_1) = f_1(y + \lambda_1 x) + f_2(y + \lambda_2 x) \tag{29}$$

where, f_i's, $i = 1, 2$ are arbitrary functions. Now to determine these arbitrary functions f_i's, we follow two (exact and approximation) approaches:

(a)**Exact approach:** Applying the IC and BC into (29) we have,

$$f_1(\pm 1 + \lambda_1 x) + f_2(\pm 1 + \lambda_2 x) = 0, \quad f_1(y \pm \lambda_1) + f_2(y \pm \lambda_2) = 0. \tag{30}$$

Obtaining two arbitrary functions f_1 and f_2, there are four equations. This exact approach for finding the arbitrary functions has great challenges and therefore we avoid it.

(b) **Approximation approach:** To overcomes this challenges, we approximated f_1 and f_2 as follows:

(i) Both f_1 and f_2 are linear functions containing arbitrary constants c_1 and c_2 as $f_1(y) = c_1 y + c_2, \quad f_2(y) = c_3\, y + c_4$. For the given B.C, this linear choice is inconsistent.

(ii) Next we consider one of f_1 or f_2 are nonlinear and another linear function. Let us consider $f_1(y) = c_1 y^2 + c_2\, y, \quad f_2(y) = c_3\, y + c_4$. Using boundary conditions (26) we have the initial guess as $u_0(x, y) = 0$. Besides one may consider both as nonlinear.

iv. **Construction of homotopy equation and iterative scheme:** From (12) we have the homotopy iterative scheme for this case, for $m \geq 1$, as follows:

$$u_m = \chi_m u_{m-1} - \mathcal{L}^{-1} R_{m-1} [\vec{u}_{m-1}] + c_1(y + \lambda_1 x)^2 + c_2 y + c_3(y + \lambda_2 x) + c_4 \tag{31}$$

where, $R_{m-1} [\vec{u}_{m-1}]$ is known as homotopy residual or corrections defined in (9) and the arbitrary constant c_i's in (31) will be computed using the boundary conditions

$$u_m (x, \pm 1) = 0, \; u_m (\pm 1, y) = 0 \tag{32}$$

v. **Successive approximation:** We apply the iterative scheme (31) with the boundary (32) into the symbolic computation software such as MATHEMATICA, MAPLE, SAGEMATH, and other and compute successive approximate solutions. For example, the first approximation is

$$\begin{aligned} u_1(x, y, \lambda_1, \lambda_2) =& e^{-\lambda_1 - \lambda_2}\gamma(-e^{\lambda_1}(-1 + e^{2\lambda_2})(-1 + x^2)\lambda_1^2 + 2e^{\lambda_2}(1 - 2e^{(1+x)\lambda_1} - x \\ &+ e^{2\lambda_1}(1 + x))y\lambda_2 + \lambda_1(-2e^{\lambda_1}(1 - 2e^{(1+x)\lambda_2} - x + e^{2\lambda_2}(1 + x))y \\ &+ e^{\lambda_2}(-1 + e^{2\lambda_1})(-1 + x^2)\lambda_2))/\, 4y\lambda_1(\lambda_1 - \lambda_2)\lambda_2 \end{aligned} \tag{33}$$

vi. **Series formulation:**

Finally summing up the successive iterations including the initial approximation, we obtain 1st order truncated series as $u(x, y, \lambda_1, \lambda_2) \approx u_0 + u_1$

vii. **Computation of optimal roots and hence optimal auxiliary linear operator:** From the previous step, it is clear that the solution u contains unknown auxiliary roots λ_1 and λ_2. To compute λ_1 and λ_2, we follow section-2.1.3. and computed the optimal values $(\lambda_1^*,\ \lambda_2^*)$ at first order. We continue up to 5th order and noted these values along with minimum residual in Table-1 (under case-A). We also compute the solution by considering $\lambda_2 = 0$ in (14a), that is, one unknown auxiliary root based A.L.O. This represents a special case of the general A.L.O (14a), and is denoted as Case-B. The corresponding residual error and CPU time are also reported in same Table-1 under Case-B.

Table 1: Convergence test of the OM-HPM at different orders (m) for the problem (26) with $\lambda = 1.68734$ for two unknowns (case-A) and one unknown (case-B) based A.L.Os.

m	Case-A			Case-B		
	$(\lambda_1^*,\ \lambda_2^*)$	Min Δ_m	CPU time (sec)	Optimal λ_1^*	Min Δ_m	CPU time (sec)
1	$(-2.7305, -2.14285)$	1.03×10^{-9}	0.9	-1.32280	1.24×10^{-8}	0.7
3	$(-0.4698, -0.28497)$	5.70×10^{-10}	91.2	-1.14094	9.31×10^{-10}	35.3
5	$(-0.19233, -0.2498)$	6.33×10^{-12}	214.3	-1.37133	2.40×10^{-12}	85.6

It is worthy to note from Table-1 that our first order OM-HPM solution is enough for the desired accuracy of 10^{-8} with CPU time less than one minute. Now, when the iteration progresses, the residual error gradually decreases for both the cases, but required CPU times for case-A is exponentially increased compared to case-B, indicating that case-B is more efficient. This observation is also noted in our earlier studies for ODEs [31, 32, 34] as well as Liao [7]. Therefore, again we strongly suggest to consider less number of unknowns (preferably one unknown). Hereafter, we continue with one parameter based A.L.O. Finally, from Table-1, the optimal form of the A.L.Os for both case-A and case-B becomes, respectively, as

$$\mathcal{L}[u] = \frac{\partial^2 u}{\partial x^2} + 0.44213\frac{\partial^2 u}{\partial x \partial y} + 0.048044\frac{\partial^2 u}{\partial y^2}, \text{ and } \mathcal{L}[u] = \frac{\partial^2 u}{\partial x^2} + 0.97403\frac{\partial^2 u}{\partial x \partial y}. \tag{34}$$

Note that, this optimal form is at the 5th order, it updated as per order of approximation, desire accuracy, parameters as well as IC and BC, which indicate that our A.L.O is dynamic. Therefore, it is endorsed here that a second order PDEs can be solved using a second order A.L.O only. While, Liao [26] proved that second order linear operator ($c_4 = 0$ in (27)) is ineffective, therefore suggested to fourth and sixth orders linear operators.

Furthermore, we also compute HAM solutions using the Liao [26] linear operator as noted in (27), by considering $c_4 = 0$ or $c_2 = 0$ and prepare Table-2. With second linear operator ($c_4 = 0$ in (27)) the solution slowly diverges and hence become ineffective, while fourth order linear operator ($c_2 = 0$ in (27)) converges but at a very slow rate. Therefore, our OM-HPM is more general and efficient than HAM. The superior accuracy of OM-HPM arises from the use of optimal auxiliary roots, which yield an exponentially decaying basis (33) that minimizes the truncation error of the series.

Example-4.1.2: Next we consider the nonlinear 1D Burger's equation in non-dimensional form [38, 41] as

$$\begin{cases} \frac{\partial u}{\partial t} + u\frac{\partial u}{\partial x} - \frac{1}{Re}\frac{\partial^2 u}{\partial x^2} = 0, \quad 0 < x < 3,\ 1 \le t \le 2 \\ u(0,t) = 0 \text{ and } u_x(0,t) = \frac{1}{t} - \frac{\pi^2 Re}{2t^2} \end{cases} \tag{35}$$

Table 2: Convergence test of the HAM at different orders (m) for the problem (26) with $\lambda = 1.68734$ for the linear operator (27) with considering $c_4 = 0$ or $c_2 = 0$.

m	when $c_4 = 0$			when $c_2 = 0$		
	Optimal c_2	Min Δ_m	CPU time (sec)	Optimal c_4	Min Δ_m	CPU time (sec)
1	-1.7614	1.02×10^{-2}	0.01	-0.5473	6.43×10^{-2}	0.03
5	-2.5076	1.15×10^{-2}	0.08	-0.3144	9.07×10^{-3}	1
10	-5.3545	1.23×10^{-2}	0.1	-0.2763	1.83×10^{-3}	4.1
20	10.5021	1.89×10^{-2}	3	-0.2494	2.85×10^{-4}	11.5

whose exact solution is $u(x,t) = \frac{x}{t} - \frac{\pi}{t}\tanh\left(\frac{x\pi Re}{2t}\right)$.

Given its complexity, various numerical and semi-analytical methods have been developed, including DTM [3], ADM [54], and HPM [41]. The given problem (35) is a simplified form of the N–S equation. By setting $\lambda_2 = 0$ in equation (14a), we consider one parameter (λ_1) based A.L.O for independent variable pairs (x,t) with $u_0(x,t) = f_1(t + \lambda_1 x) + f_2(t)$, where f_1 and f_2 are arbitrary functions. Similar to previous example (step-iii), we follow these two procedures:

i. Exact approach for arbitrary functions: Applying the given conditions (35) into the general solution we have $u_0(0,t) = f_1(t) + f_2(t) = 0$, and $u_{0_x}(0,t) = \lambda_1 f_{1_x}(t) = \frac{1}{t} - \frac{\pi^2 Re}{2t^2}$ After solving these equations we have f_1 and f_2, finally we have the initial guess as $u_0(x,t) = \frac{2-\pi^2 Re}{2\lambda_1}\log\left(\frac{t+\lambda_1 x}{t}\right)$.

The m^{th} order homotopy derivative of the given nonlinear equation (35) be defined as

$$\mathcal{R}\left[\vec{u}_m(x,t)\right] = \frac{\partial u_{m-1}}{\partial t} + \sum_{k=0}^{m-1} u_k \frac{\partial u_{m-1-k}}{\partial x} - \frac{1}{Re}\frac{\partial^2 u_{m-1}}{\partial x^2} \tag{36}$$

Using these components into the m^{th} order homotopy equations (11)-(12), we successfully computed the solution up to two iterations. However, higher order iterations ($m > 2$) could not be performed because the singularity is introduced due to the logarithmic basis function. Now, if we consider up to 2nd order iterations and compute the optimal value of unknown auxiliary root λ_1 by minimizing the residual error (17) we found the optimal value of λ_1 as $3.74 \times 10^{-7} \approx 0$. Therefore, our linear operator (14a) with this optimal value of λ_1 is similar to that considered by Biazar and Ghazvini [41], Biazar and Aminikhah [42], which is

$$\mathcal{L}u = \frac{\partial^2 u}{\partial x^2} \tag{37}$$

ii. Approximated approach: In order to embed this parameter (optimal λ_i's) into the A.L.O or/and solution. We consider the arbitrary functions f_1 and f_2 as any arbitrary polynomial function with arbitrary constant as coefficient. Though, there are numerous choices of f_1 and f_2, let us consider initially both the functions f_1 and f_2 are linear:

$$f_1(x,t) = A(t + \lambda_1 x),\ f_2(t) = Bt \text{ and hence } u_0(x,t) = A(t + \lambda_1 x) + Bt \tag{38}$$

with A and B are arbitrary constants. Now, using the conditions (35) we have the initial approximation as

$$u_0(x,t) = \frac{x}{t} - \frac{\pi^2 x Re}{2t^2} \tag{39}$$

which is the same as Biazar and Ghazvini [41], Biazar and Aminikhah [42] with the linear operator (37). It is to note that, the general solution (38) for the $u_0(x,t)$ is obtained by solving $\mathcal{L}[u] = 0$, but

Table 3: Optimal values of controlling parameters embedded in the respective methods (OVIM, Optimal HAM, and OH-HPM), along with the corresponding minimum residuals (Δ_m) for the Example-4.1.2

order m	Re	OVIM		Optimal HAM		OM-HPM	
						Case-A	
		$\hbar^*$	Δ_m	$\hbar^*$	Δ_m	λ_1^*	Δ_m
5	0.222	0.01961	1.049×10^{-3}	-0.40079	8.912×10^{-4}	-0.04283	1.785×10^{-19}
	1	0.01961	2.125×10^{3}	-0.03449	4.208×10^{2}	-0.58552	2.738×10^{-8}
	2	0.01961	8.503×10^{3}	-0.00916	3.227×10^{4}	-0.87349	3.402×10^{1}
10	0.222	0.31644	7.075×10^{-5}	-0.44137	3.483×10^{-7}	-0.03544	1.163×10^{-32}
	1	0.01642	1.334×10^{2}	-0.03931	4.839×10^{1}	-0.56735	1.805×10^{-11}
	2	0.03862	5.492×10^{2}	-0.01041	4.789×10^{3}	-0.93226	5.761×10^{-1}
15	0.222	0.31789	1.663×10^{-7}	-0.46105	4.578×10^{-10}	-0.03445	1.163×10^{-36}
	1	0.01178	1.185×10^{2}	-0.03714	2.745×10^{1}	-0.56096	6.448×10^{-16}
	2	0.04678	5.165×10^{2}	-0.01183	3.813×10^{2}	-0.93960	3.068×10^{-3}

after imposing I.C, $u_0(x,t)$ as noted in (39), does not satisfy $\mathcal{L}[u_0] = 0$. Although this is contrary to the conventional HAM/HPM framework, it should be noted that $u_0(x,t)$ satisfies the given I.C. In the context of homotopy, this is reasonable, because, in the homotopy frame the initial solution continuously deforms to the final solution, and therefore, any entire function satisfying the I.C/B.C can be treated as a valid initial solution. Therefore, in the frame of homotopy methods, for PDE satisfying $\mathcal{L}[u_0(x,t)] = 0$ is a weak condition, whereas satisfying the I.C/B.C for $u_0(x,t)$ constitutes a strong condition.

Using the A.L.O and the initial approximation (39) into the m^{th} order homotopy equations (11)-(12) we successively compute iterations. First order iterations is

$$u_1(x,t) = -\frac{\pi^4 \mathrm{Re}^3 x(1 - e^{\lambda_1 x} - \lambda_1 x)}{4\lambda_1^2 t^4} \tag{40}$$

It is seen that, our solutions $u_1, u_2, \ldots$ contain our controlling parameter λ_1. We continue up to 15th order successive approximations and then prepare Table-3. It is worthy to note from Table-3 that λ_1 becomes non-zero, by which we minimize the residual error (17) and optimize the solution. We also compute the series solution with those of the advanced semi-analytical methods: Optimal HAM [7, 30] and OVIM [38, 42] with the linear operator (37) and the corresponding initial approximation (39) as of Moghimi and Hejazi [38], Biazar and Ghazvini [41], Biazar and Aminikhah [42]. Similarly, the optimal value of controlling parameter $\hbar$ ($\hbar^*$) and minimum of residual error Δ_m (17) of Optimal HAM and OVIM are presented in Table-3.

Now, if we compare the residual error of our OM-HPM solutions with those of Optimal HAM and OVIM, we see that both the Optimal HAM and OVIM are convergent only at a very low Re, particularly for $Re = 0.222$. However, they fail to converge as Re increases, especially for $Re = 1$ and $Re = 2$, over the specified domain $0 < x < 3$ and $1 \leq t \leq 2$, where the residual errors become significantly large (of the order of 10^2), thereby violating the sufficient conditions for convergence (Section-2.4). On the other hand, at a fixed Re, the residual error (17) progressively decreases with increasing order of approximation, thereby satisfying the sufficient conditions for convergence and also ensured stability [6]. Therefore, our OM-HPM provide convergent solution for all the values of Re considered here.

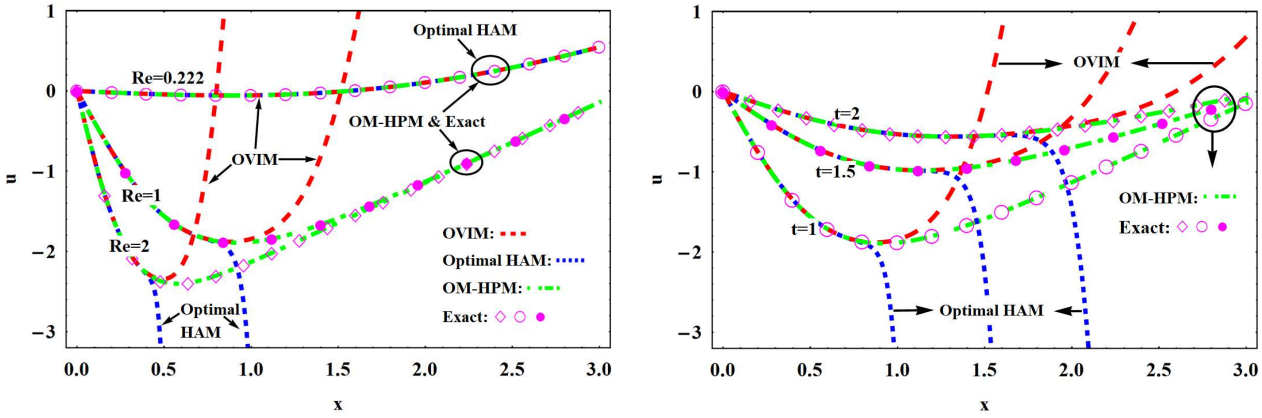


Fig. 3: Comparison of computed semi-analytical solutions with the exact solution and contemporary methods (Optimal HAM and OVIM): (a) for varying Re at fixed $t = 1$; (b) for varying t at fixed $Re = 1$.

The computed semi-analytical solution by propose OM-HPM along with contemporary methods (optimal HAM and optimal VIM) are presented in Fig.3. From the Fig.3(a) it is evident that when Re is too small ($Re = 0.222$) our solution and the solutions by those of optimal HAM and optimal VIM are agreeing with the exact solution throughout the domain. But when the Re is increased and equal to $Re = 1$ or $Re = 2$, the solutions by those of contemporary methods (optimal HAM and optimal VIM) are not matching with the exact solution in the whole domain. That is, when the Re increases, the domain of convergent decreases for the optimal HAM and optimal VIM, and is divergent beyond certain domain. From Fig.3(b) we see that when the time increase, the velocity decrease and the effective domain of convergence of optimal HAM and optimal VIM increase. However, it is clear that when the velocity is very low (near equal to zero) the optimal HAM and optimal VIM solution agrees with the exact solution throughout the domain, while for the non-zero velocity the optimal HAM and optimal VIM provides local series solution. Therefore, the solution with those of optimal HAM and optimal VIM are useless to analyse flow properties of a fluid. On the other hand, the domain of convergence of our OM-HPM does not alter with the Re or time. It may be noted that when Re increases the convective term of N-S equation (35) becomes dominant. The proposed OM-HPM successfully captures this nonlinear effect even at $Re = 2$, which is ten times higher than the value considered in the optimal HAM and OVIM approaches. It is noteworthy that this superiority of the OM-HPM arises mainly from the optimal choice of $\mathcal{L}$ at each m, which ensures a better homotopy and consequently an optimal series solution. This again confirms that the optimal selection of $\mathcal{L}$ and u_0 play far more crucial role than the artificial auxiliary parameters used in HAM and OVIM, which is consistent with the conclusion made by Liao [6, 7, 25], Van Gorder [40], and our previous observation [31–33].

[41] and [38] have used the following auxiliary linear operator

$$\mathcal{L}u = \frac{\partial u}{\partial t} \tag{41}$$

and reported the similar solution as the linear operator (37) of the optimal VIM and optimal HAM discussed here. We have also verified the same. Moreover, this problem is defined on a small domain, $0 < x < 3$. Then, neither the optimal VIM nor the optimal HAM can provide a solution that remains valid across the entire domain. This again validates the observation of Liao [6] that a linear operator whose base function is polynomial (that is, all $\lambda_i = 0$) produces only a local solution.

4.2. **ROM-HPM for pressure linked INSEs:**

This section presents the application of ROM-HPM to pressure-linked full INSEs (1a)-(1c) without any reduction and consideration. Based on whether the pressure is known or unknown, the section is divided into two subsections as follows:

4.2.1. **When pressure gradients are known:**

Here we consider the classical fluid dynamical problem, which is known as Couette-Poiseuille (C-P) flow [13, 15, 20], where the pressure gradients are known and the flow is steady ($\frac{\partial}{\partial t} = 0$). Let, $-\frac{\partial p}{\partial x} = P_x$ and $-\frac{\partial p}{\partial x} = P_y$, where P_x and P_y are known. *Under several assumptions, such as (i.) flow is one-dimensional, i.e.* $v = 0, \frac{\partial u}{\partial y} = 0$, *and* $\frac{\partial p}{\partial y} = 0$, *(ii.) flow is fully developed, i.e.* $\frac{\partial u}{\partial x} = 0$, *etc.* the exact solution of the problem (1a)-(1c) subjected to the following boundary condition [13, 15, 20]

$$y = 0 : u(x,0) = 0, v(x,0) = 0, \text{ and } y = 1 : u(x,1) = 1, v(x,1) = 0 \tag{42}$$

is computed as

$$u(x,y) = y + \frac{ReP_x}{2} y\,(1-y)\,, \text{ and } v(x,y) = 0 \tag{43}$$

Needless to mention that the above solution is computed by removing the highly non-linear terms of N-S equation. In contrast, our current objective is to compute a semi-analytical solution to the full INSE (Eqs.(1a)-(1c)) without any simplifications. As the pressure gradients are assumed to be known, so the additional algorithm for the pressure correction is not needed.

Based on the earlier observations, we considered the linear operators $\mathcal{L}_1$ and $\mathcal{L}_2$ for u and v, respectively as

$$\mathcal{L}_1[u] = \frac{\partial^2 u}{\partial x^2} - \lambda_1 \frac{\partial^2 u}{\partial x \partial y}, \text{ and } \mathcal{L}_2[v] = \frac{\partial^2 v}{\partial x^2} - r_1 \frac{\partial^2 v}{\partial x \partial y} \tag{44}$$

along with the corresponding general initial approximations u_0 and v_0 given as

$$u_0(x,y,\lambda_1) = f_1(y + \lambda_1 x) + f_2(y), \text{ and } v_0(x,y,r_1) = g_1(y + r_1 x) + g_2(y) \tag{45}$$

Now, to determine the arbitrary functions in u_0 and v_0 (45) we initially followed the exact approach for getting arbitrary functions f_i and g_i. However, although a sufficient number of conditions are available, determining the arbitrary functions is highly complex. Furthermore, introducing additional BC, such as inlet conditions, makes this approach more complex. Therefore, we completely discard this approach for further study and followed the approximated approach. As per the choices of f_i, we consider the following three possible cases:

(A). Both functions f_1 and f_2 are linear: Let us consider $f_1(x,y) = c_1(y + \lambda_1 x)$ and $f_2(y) = c_2 y$, where c_1 and c_2 are arbitrary constants. Satisfying the given BC (42) we have

$$u_0(x,y) = y, \; v_0(x,y) = 0 \tag{46}$$

which is the exact solution of the Couette flow (with $P_x = 0$ in equation (43)). Similarly, we compute successive OM-HPM corrections as

$$u_1(x,y) = 0, \; v_1(x,y) = 0; \; u_2(x,y) = 0, \; v_2(x,y) = 0 \tag{47}$$

That is, there is no correction. Because, the initial approximation gives one of the exact solution of the problem. Hence, the approximated solution becomes of the form

$$u(x,y) = \sum_{m=0}^{\infty} u_m = y, \; v(x,y) = \sum_{m=0}^{\infty} v_m = 0 \tag{48}$$

Therefore, we computes only a special (Couette flow) solution, and we fail to compute the C-P flow solution. This disorder happens due to improper choices of initial approximation. We also testified several other choices of linear forms of f_1 and f_2 including time dependent ($f_1(y,t) = c_1(t + \lambda_1 y)$ and $f_2(t) = c_2 t$) and observed the same.

(B). Function f_1 is linear but f_2 is nonlinear: Next consider $f_1(x,y) = c_1(y + \lambda_1 x)$ and $f_2(y) = c_2\, y^2$, substituting BC (42) we compute

$$u_0(x,y) = y^2,\ v_0(x,y) = 0 \tag{49}$$

These satisfy I.C/B.C and $\mathcal{L}[u] = 0$. Now with this initial guess (49) we compute successive OM-HPM corrections, and first approximation is

$$u_1(x,y) = \frac{(-1+y)y(-2+RePx)(1-\mathrm{e}^{x\lambda_1}+x\lambda_1)}{Re\ x\lambda_1^3},\quad \text{and}\quad v_1(x,y) = 0. \tag{50}$$

We continue up to 10th iterations. For the accuracy of the computed solution, we plot Fig.4 for Couette flow ($P_x = 0$). From Fig.4(a) we see that though the computed solution $u(x,y)$ is a function of x and y (ref. Eq.(50)) but the contribution of x is negligible and the solution agrees with the exact solution with a maximum relative error 0.13%. From Fig.4(b) we see that our solutions at higher Re ($= 10$ & 15) slightly deviate from the exact solution of Couette flow ($u = y$) only at $x = 0.1$, that is, $u = u(x,y,Re)$ at $x = 0$. In fact, after substituting $P_x = 0$ in the expression (50), we see $u = u(x,y,Re)$. However, it is worthy to note that beyond $x = 1$, our computed solution at $P_x = 0$ completely matches with the exact $u = u(y)$ (Eqn.(43)).

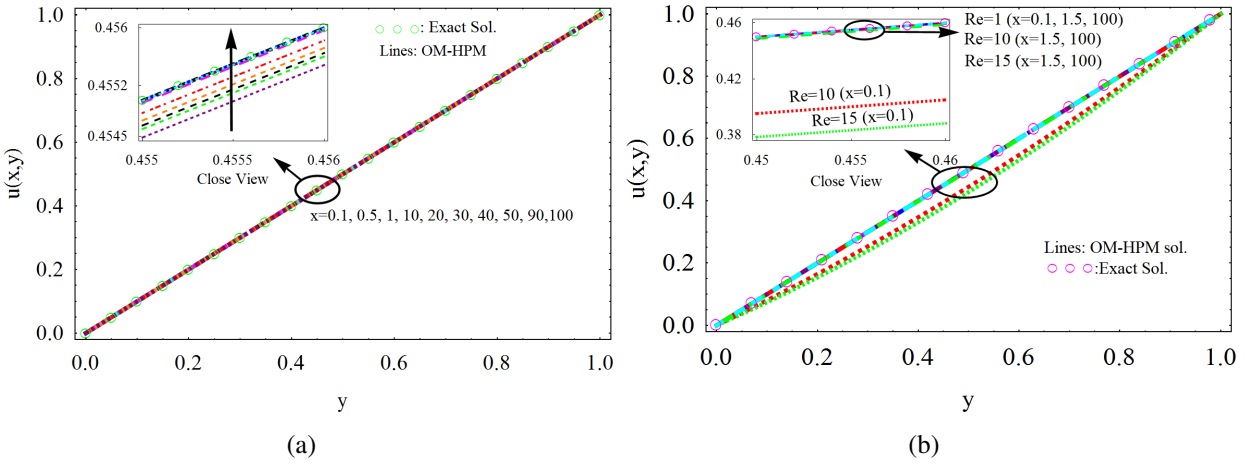


Fig. 4: Comparison of computed solutions for the problem (42) under case-B with the exact Couette flow solution (Eq.(43) with $P_x = 0$): (a) velocity profiles at different axial positions x; (b) profiles for different Re.

A similar exercise is also done in Fig.5 for the C-P flow when $P_x \neq 0$. From both Fig.5(a) and Fig.5(b) it is seen that the computed solution is agreeing with the exact solution for the channel length $x \geq 1.5$ with maximum relative percentage error 3.22%. It may be noted that Re and P_x are mechanically similar [16] and it is reflected in our solution. While before development of flow $x < 1.5$ this error is very high. It is physically plausible that physically the flow is not fully developed from the inlet, flow becomes developed after certain distance of the channel (beyond $x = 1.5$) [17]. Mathematically, though our solution expression (50) is $u = u(x,y,Re,P_x)$, but after certain

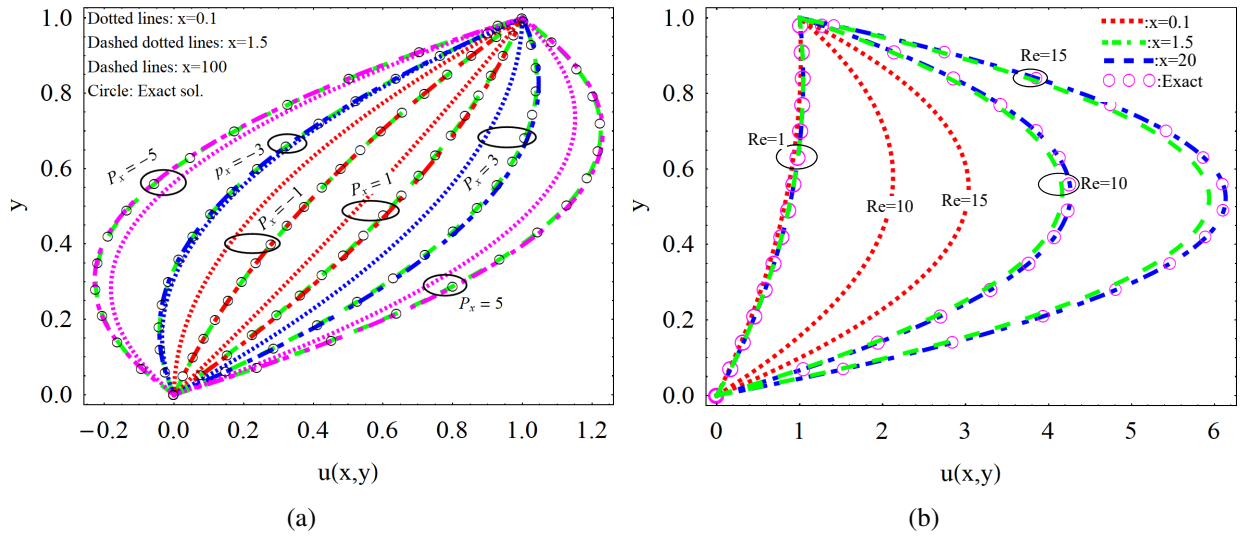


Fig. 5: Comparison of the computed semi-analytical solution (lines) for the problem (42) under case-B with the exact solution (hollow circles) of C-P flow (Eq.(43) with $P_x \neq 0$) (a) velocity profiles for different pressure gradient P_x $(= \pm 1, \pm 3, \pm 5)$ and different x $(= 1, 1.5, 100)$ at fixed $Re = 1$; and (b) profiles for different Re $(= 1, 10, 15)$ and different x $(= 1, 1.5, 20)$ at fixed $P_x = 3$.

$x(> 1.5)$, u-velocity becomes independent of x and exactly matches to the expression (43) of the exact solution of C-P flow for different Re and P_x. Therefore, it may be deduced that our solution of complete INSE with highly nonlinear terms completely matches with the exact solution of C-P flow (43) , which are computed based on several assumptions, like, neglecting non-linear terms. In other words, our propose method could handle the INSE and nullify the contribution of non-linear terms of INSE to such physical problems where it has negligible contribution.

(C). Both functions f_1 and f_2 are nonlinear

Finally, we also consider $f_1(x, y) = c_1(y + \lambda_1 x)^2$ and $f_2(x, y) = c_2\, y^3$. By satisfying the given BC (42), we obtain

$$u_0(x, y) = y^3, \; v_0(x, y) = 0 \tag{51}$$

Similarly, with this initial approximation (51) into the mth order homotopy equations (11)-(12) we compute successive 10th OM-HPM iterations. Substituting optimal value of λ_1, we have the final velocity whose profiles are compared with the exact one (not presented here due to brevity). As can be seen here that qualitatively similar to Figs.4 and 5, respectively. It is also seen that the flow development or, the value of x at which u becomes independent of x is dependent on the value of P_x or Re. While comparing the results between these two cases (case-B and case-C), it may be deduced that case-B gives faster solution. This is due to the fact that here the exact solution is quadratic polynomial in y, which is the initial approximation of case-B, while the initial approximation for case-C is cubic polynomial.

Similar to our earlier studies on ODEs [32, 33], the OM-HPM also provides a globally convergent series solution (valid over the entire domain $x > 0$) for the PDEs. Thereby eliminating the need for an artificial outlet boundary to define the channel length, which required for numerical CFD computation. It is noteworthy that this globally convergence arises despite the truncation error associated with the homotopy truncation (neglect high order terms of a finite iteration). In our previous studies [33], it was shown that the optimal linear operator of our OM-HPM produces

exponential basis functions, and the same is also observed here (ref. Eq.(50)). Consequently, unlike to the conventional HAM/HPM whose solutions are often finite degree polynomial base, the OM-HPM solution is not itself a Taylor series, but its solution can be expressed as an infinite power series that reproduces the exact Taylor expansion of the exact solution at any finite iteration [34].

4.2.2. **When pressure gradients are unknown:**

In this section, we testify our proposed method ROM-HPM on the full pressure linked INSE (1a)-(1c) by considering two examples of fluid flow where pressure is unknown. First one is the 2D steady incompressible Newtonian channel flow with slip boundary conditions (section-4.2.2.1) and second one is the 2D unsteady incompressible non-Newtonian flow in microchannels with constant/variable injection/suction (section-4.2.2.2). Due to unavailability of the exact solutions, the computed semi-analytical solutions by the ROM-HPM are frequently compared with those by CFD. Finally, a comprehensive methodological comparison between ROM-HPM and CFD (both continuous and discrete forms) is presented in Section-4.2.2.3.

4.2.2.1 Newtonian and steady fluid flow in a microchannels with slip boundary conditions

We consider the following slip boundary conditions corresponding to the governing Eq.(1) with $\frac{\partial}{\partial t} = 0$ of the fluid flow in a microchannels from Kundu et al. [17]:

$$\begin{cases} y = 0(\text{at bottom wall}) : u(x,y) = u_w(x), v(x,y) = 0 \\ y = 1(\text{at top wall}) : u(x,y) = u_w(x), v(x,y) = 0 \\ x = 0(\text{at inlet}) : u(x,y) = u_{in}, v(x,y) = 0 \end{cases} \tag{52}$$

where, $u_w(x) = \frac{3}{2}\left(\frac{L_s}{\delta}\right) - \frac{1}{2}\left(\frac{L_s}{\delta}\right)^3$, $\delta = \frac{5x}{\sqrt{xRe}}$, $L_s = 0.001$ is known as slip boundary condition. Kundu et al. [17] solved the flow(governed by Eq.(1)) with the boundary condition (52) in addition to the outlet boundary at $x = 100 : \frac{\partial u}{\partial x} = 0, \frac{\partial v}{\partial y} = 0$. They solved the full N-S equations (19) numerically using the methodology described in section-3 within a finite channel. After non-dimensionalisation, the computational domain was defined over the closed boundary $0 \leq y \leq 1, 0 \leq x \leq 100$, representing a finite micro-channel. While, we attempt to solve the full N-S equations (19) analytically, subject to the BC (52), but without imposing any outlet boundary condition.

Since the pressure gradient is unknown and the problem is steady, the homotopy correction terms for the velocity components take the forms given in (20a) and (20b), with $\frac{\partial}{\partial t} = 0$. The corrected pressure gradient are to be calculated using (21a) and (21b). Here also we consider single parameter based operator (44) and its corresponding initial guess (45). There are numerous possibilities to choose the arbitrary functions f_1 and f_2 of initial approximation (45), but here we consider f_1 as linear and f_2 as nonlinear:

$$u_0(x,y,\lambda_1) = A_1(y + \lambda_1 x) + B_1 + C_1 y^2,\ v_0(x,y,r_1) = A_2(y + r_1 x) + B_2 + C_2 y^2 \tag{53}$$

where $A_1, B_1, C_1, A_2, B_2, C_2$ are arbitrary constant. In order to accommodate one additional condition (inlet) here, in comparison to previous situation (sec.4.2.1), two more additional arbitrary constants (one each for u and v) are introduced in (53). Finally, u_0, v_0 for the momentum equations takes the form

$$u_0(x,y,\lambda_1) = \frac{u_{in}y(y-1) + \lambda_1 u_w x}{y(y-1) + \lambda_1 x},\ v_0(x,y,r_1) = 0 \tag{54}$$

As per our methodology (step-2, see section-2.2) let us consider the initial pressure arbitrarily as

$$p_0(x, y) = x \tag{55}$$

Now with the linear operator (44) and the initial approximations (54) and (55), we apply ROM-HPM (ref. Section-2.2) and compute successive approximations. First approximation is

$$\begin{aligned}
u_1(x, y, \lambda_1, r_1) = &\{(-1+y)y(-1+e^{x\lambda_1} - x\lambda_1)(\lambda_1 x \mathrm{Re}((-1+y)\, y + x\lambda_1)^2 - 2u_{\text{in}}(-(-1+y)y \\
&+x(-2-y+y^2)\lambda_1 + 5x^2\lambda_1^2) + 2u_w(-(-1+y)y + x(-2-y+y^2)\lambda_1 + 5x^2\lambda_1^2))\} \\
&/\lambda_1^3 x \mathrm{Re}((-1+y)y + x_1)^2((-1+y)y^2 + \lambda_1 x) \\
v_1(x, y, \lambda_1, r_1) = &\, 0, \\
p_1(x, y, \lambda_1, r_1) = &-\frac{(u_{\text{in}} - u_w)(2(-1+y)y + x\lambda_1 - \frac{(1-2y)^2(-1+y)y}{((-1+y)y+x\lambda_1)^2} + \frac{2(1-5y+5y^2)}{(-1+y)y+x\lambda_1})}{\lambda_1 Re}.
\end{aligned}$$

We compute up to $m = 10$th order approximations. From the solution expression we see that there is no radial velocity, that is, $v = 0$, the same was observed by Kundu et al. [17] numerically.

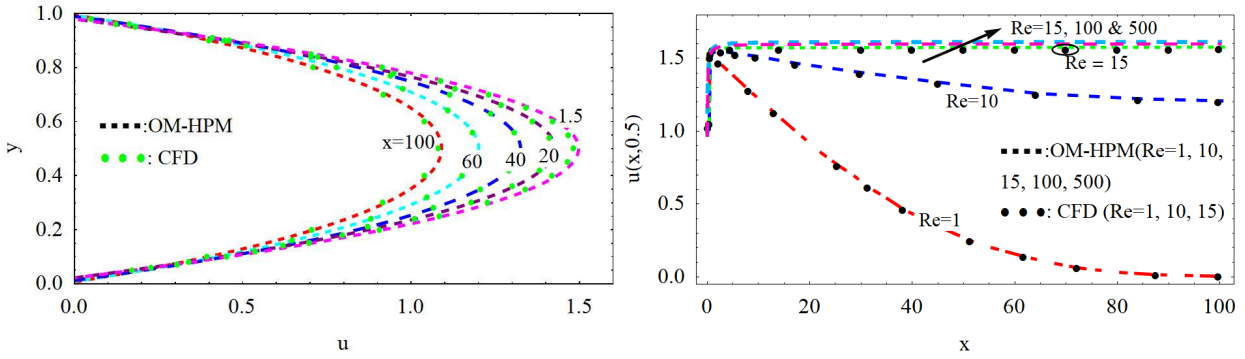


Fig. 6: Comparison of computed semi-analytical velocities with those of CFD solution by Kundu et al. [17] under slip boundary conditions ($u_w \neq 0$): (a) Axial velocity profiles ($u(x, y)$) for $Re = 10$ at different axial positions (x); (b) Centerline axial velocity $u(x, 0.5)$ for various Re ($= 1, 10, 15, 100, 500$).

In order to compare with CFD solution (of [17]), we consider the inlet value as $u_{in} = 1$ and the slip value u_w as defined in Eq.(52). In Fig.6(a) we compare the axial velocity (u) at a fixed $Re = 10$. It is evident from Fig.6(a) that our computed solution agrees with [17] very well. The maximum relative percentage error (RPE) over the whole domain is around 2.78%. From the centerline velocity distributions presented in Fig.6(b), it can be seen that our solutions at $Re = 1, 10$ and 15 show excellent agreement with the CFD solution those of [17] with a maximum RPE of only 2.16% over the entire domain for $Re = 15$. Notably, similar to [17] the ROM-HPM also successfully captures the bottleneck effect of the channel flow even at very low Re. Furthermore, as seen from Fig.-6(b), the proposed ROM-HPM remains highly accurate even at higher Re, where the residual errors are of the order of 10^{-8} and 10^{-7} for $Re = 100$ and $Re = 500$, respectively, at $m = 10$.

Table-4 presents the convergence behavior of ROM-HPM at different orders of approximation with fixed $Re = 500$ for the INSE. From Table-4, we see that at lower order ($m = 2$) there is a residual error of order 10^{-3}. However, this error decreases with the increase of m, and at $m = 10$ the error becomes of order 10^{-7}, which is the desired accuracy. In addition, our computed solution satisfies the continuity equation very well, with an error of order 10^{-7}, and the pressure satisfies

Table 4: Convergence test of ROM-HPM at different orders (m) for the INSE in (52) at $Re = 500$.

m	Residual Minimization (18)			Additional condition (25)		CPU time
	λ_1^*	r_1^*	Δ_m	Condition (i)	Condition (ii)	(min)
2	-0.751044	-1.068947	9.48×10^{-3}	4.164×10^{-2}	6.281×10^{-2}	0.8
5	-0.568362	-0.940678	9.48×10^{-6}	9.462×10^{-5}	5.726×10^{-4}	3.4
10	-0.487254	-0.814582	6.44×10^{-9}	2.301×10^{-7}	7.062×10^{-6}	22.6

the Euler condition (25) with the desired accuracy. In the same table, we also show how much CPU usage is consumed to execute different orders. As we have calculated, the CFD methodologies consume CPU time of around 40–45 minutes, while our proposed ROM-HPM consumes approximately 23 minutes. Therefore, compared to the CFD methodologies, our proposed technique is more efficient for analyzing the flow phenomena.

4.2.2.2 Non-Newtonian and un-steady flow in a microchannels with variable injection/suction

Finally we consider a 2D unsteady incompressible non-Newtonian flow in a microchannels with variable injection/suction for which the N-S equation in non-dimensional (Mondal and Maiti [16], except the magnetic field and energy equation) are

$$Re_u \frac{\partial u}{\partial x} + Re_v \frac{\partial v}{\partial y} = 0, \tag{56a}$$

$$\frac{\partial u}{\partial t} + u\frac{\partial u}{\partial x} + \frac{Re_v}{Re_u} v \frac{\partial u}{\partial y} = -\frac{\partial p}{\partial x} + \frac{1}{Re_u}\left[\frac{\partial}{\partial x}\left(2\frac{\mu_{af}}{\mu_f}\frac{\partial u}{\partial x}\right) + \frac{\partial}{\partial y}\left\{\frac{\mu_{af}}{\mu_f}\left(\frac{\partial v}{\partial x} + \frac{\partial u}{\partial y}\right)\right\}\right] \tag{56b}$$

$$\frac{\partial v}{\partial t} + \frac{Re_v}{Re_u} u \frac{\partial v}{\partial x} + \left(\frac{Re_v}{Re_u}\right)^2 v \frac{\partial v}{\partial y} = -\frac{\partial p}{\partial y} + \frac{1}{Re_u}\left[\frac{\partial}{\partial y}\left(2\frac{\mu_{af}}{\mu_f}\frac{\partial v}{\partial y}\right) + \frac{\partial}{\partial x}\left\{\frac{\mu_{af}}{\mu_f}\left(\frac{\partial v}{\partial x} + \frac{\partial u}{\partial y}\right)\right\}\right] \tag{56c}$$

where

$$\mu_{af} = \mu_f \left[2\left\{\left(\frac{\partial u}{\partial x}\right)^2 + \left(\frac{\partial v}{\partial y}\right)^2\right\} + \left\{\frac{\partial u}{\partial y} + \frac{\partial v}{\partial x}\right\}^2\right]^{\frac{\alpha-1}{2}} \tag{57}$$

μ_f is the viscosity, α is power-law index, $Re_u = \frac{U_0 a \rho_f}{\mu_f}$, $Re_v = \frac{V_0 a \rho_f}{\mu_f}$. Here, U_0 and V_0 are the dimensional velocities at inlet and injection/suction, respectively, ρ_f is the density of fluid and 'a'is the channel width. The boundary conditions for variable injection/suction to/from the porous walls [16] are:

$$y = 0 \text{ (at bottom wall)} : u(x, y) = 0,\ v(x, y) = v_B(x, t) \tag{58a}$$

$$y = 1 \text{ (at top wall)} : u(x, y) = 1,\ v(x, y) = v_T(x, t) \tag{58b}$$

$$x = 0 \text{ (at inlet)} : u(x, y) = y + Re_u P_x\, y(1 - y),\ v(x, y) = 0 \tag{58c}$$

Where, $v_B(x, t)$ and $v_T(x, t)$ are the non-dimensional variable injection-suction function at bottom and top walls, respectively. P_x is non-dimensional pressure gradient at the inlet due to the classical C-P flow. These BCs are for an open channel. For closed channel, one has to prescribe an additional artificial boundary at the outlet. Mondal and Maiti [16] studies using the methodology as described

in section-3, subject to the additional artificial boundary at the outlet as $x = 25 : \frac{\partial u}{\partial x} = 0, \frac{\partial v}{\partial y} = 0$. While, we solve this problem directly using ROM-HPM without any artificial outlet boundary. Here also we consider one unknown parameter based linear operator as noted in (44) and both arbitrary functions in initial guess u_0 (45) f_1 and f_2 as linear:

$$u_0(x,y,t,\lambda_1) = A_1(y+\lambda_1 x+t)+B_1 t+C_1(y+t),\ v_0(x,y,t,r_1) = A_2(y+r_1 x+t)+B_2 t+C_2(y+t) \tag{59}$$

where $A_1, B_1, C_1, A_2, B_2, C_2$ are arbitrary constants. The initial approximation for u and v subjected to BC (58) with the guess pressure becomes

$$u_0(x,y,t,\lambda_1) = y + Re_u P_x y(1-y),\ v_0(x,y,t,r_1) = \frac{r_1 x}{r_1 x - y(1-y)}(v_B - y^2 v_B + y^2 v_T),$$
$$p_0(x,y,\lambda_1) = x. \tag{60}$$

It is worth noting that in the absence of injection or suction ($v_B = v_T = 0$), the initial approximation reduces to the classical C-P flow, which is consistent with our earlier discussion in Section-4.2.1. Using the ROM-HPM, we compute successive approximations. The first approximation is as follows:

$$u_1(x,y,t,\lambda_1,r_1) = \frac{1}{\lambda_1}\Bigg\{(1-y)(1+\frac{(1+PRe_u)\mathrm{Re_v} v_B}{Re_u} + 2P((1+P_x Re_u)^2 + 2a_{v_B}^2)^{\frac{1}{2}(-3+\alpha)}$$
$$((1+PRe_u)^2\alpha + 2a_{v_B}^2))(-x+\frac{-1+e^{x\lambda_1}}{\lambda_1})\Bigg\} + \frac{1}{\lambda_1}\Big\{y(1+v_B+2P_x((-1+PRe_u)^2 +$$
$$\cdots + \frac{\mathrm{Re_v}(-1+P_x Re_u(-1+2y))((-1+y)v_B + y\, v_T)x}{Re_u(r_1 x - y(1-y))^3})(-x+\frac{-1+e^{x\lambda_1}}{\lambda_1})\Bigg\} \tag{61a}$$

$$v_1(x,y,t,\lambda_1,r_1) = \frac{4v_B PRe_u(-1+P_x Re_u)y((-1+P_x Re_u)^2 + 2a^2)^{\frac{1}{2}(-3+\alpha)}(-1+e^{x\lambda_2} - xr_1)}{Re_u(r_1 x - y(1-y))^3}$$
$$+\frac{4v_B P_x Re_u(1+P_x Re_u)(-1+y)(-1+\alpha)((1+P_x Re_u)^2 + 2a^2)^{\frac{1}{2}(-3+\alpha)}(-1+e^{xr_1} - r_1 x)}{r_1^2}$$
$$-\frac{v_B}{r_1^2}\Big\{4P_x Re_u(-1+P_x Re_u(-1+2y))(-1+\alpha)((-1+P_R e_u(-1+2y))^2 + 2a^2)^{\frac{1}{2}(-3+\alpha)}$$
$$(-1+e^{xr_1} - xr_1)\Big\} \tag{61b}$$

$$p_1(x,y,t,\lambda_1,r_1) =$$
$$x((\mathrm{v_B}+\mathrm{v_T})(-1+P_x Re_u(-1+y))y - \frac{\mathrm{Re_v}(\mathrm{v_B}(-1+y)+\mathrm{v_T}y)(-1+P_x Re_u(-1+2y))x}{Re_u(r_1 x - y(1-y))^2}$$
$$-2P(2\mathrm{v_B}^2 + (-1+P_x Re_u(-1+2y))^2)^{\frac{1}{2}(-3+\alpha)}(2\mathrm{v_B}^2 + (-1+P_x Re_u(-1+2y))^2\alpha)) \tag{61c}$$

and continued upto 5th order approximations. From the solution expression it is to note that though we consider the governing equations as unsteady but the solution becomes steady, the same was observed numerically by Mondal and Maiti [16]. Moreover, under no injection-suction ($v_B = 0 = v_T$) as can be seen from the above expression (61b) that $v = 0$, which matches with our previous section solution. Now we compute the optimal values (λ_1^*, r_1^*) of unknown auxiliary roots (λ_1, r_1) at different cases, depending upon the injection-suction:

Table 5: Optimal values of unknown auxiliary roots (λ_1^*, r_1^*) along with corresponding minimum residual errors (Δ_5) for the problem (56) at the 5th-order ROM-HPM solution for different values of α.

α	Case-A: Constant injection				Case-B: Variable injection-Suction			
	$\lambda_1^*,\ r_1^*$	Δ_5	Additional Condition (25)		$\lambda_1^*,\ r_1^*$	Δ_5	Additional Condition (25)	
			(i)	(ii)			(i)	(ii)
0.5	$-0.68397, -0.62341$	1.96×10^{-11}	3.50×10^{-7}	1.53×10^{-6}	$-0.27585, -0.14758$	1.41×10^{-11}	4.73×10^{-7}	9.47×10^{-6}
0.8	$-0.43176, -0.37689$	5.99×10^{-10}	1.78×10^{-7}	1.30×10^{-6}	$-0.68397, -0.62341$	1.96×10^{-11}	8.67×10^{-7}	6.53×10^{-6}
1	$-0.27585, -0.14758$	1.41×10^{-15}	6.00×10^{-8}	5.83×10^{-7}	$-0.52176, -0.46328$	1.49×10^{-14}	1.96×10^{-7}	9.94×10^{-7}
1.5	$-0.16879, -0.39844$	6.12×10^{-11}	2.49×10^{-6}	7.90×10^{-6}	$-0.68397, -0.62344$	1.96×10^{-11}	3.84×10^{-6}	3.27×10^{-6}

Case-A: $v_T = 0,\ v_B = 0.1$: That is, constant injection from the bottom wall and impermeable at the top wall.

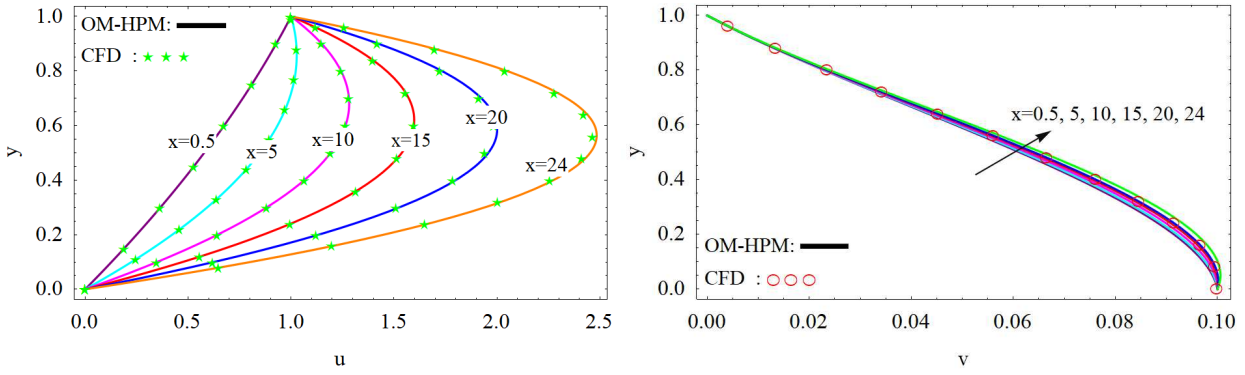
Case-B: $v_T = -0.1 \sin\left(\frac{x}{25}\right),\ v_B = 0.1$: That is, constant injection from the bottom wall and variable injection-suction from the top wall.

We set $Re_u = Re_v = 2.48$ and $P_x = 0.2$. The optimal values (λ_1^*, r_1^*) of unknown auxiliary roots λ_1 and r_1, corresponding to the minimum residual error Δ_5 for different power law fluids (α), are reported in Table-5. Based on these optimal values, a detailed convergence analysis of the ROM-HPM solutions for both Case-A and Case-B is performed. According to the necessary condition established in Section-2.4, the optimal controlling parameters attain negative values, ensuring that the higher-order homotopy terms involve decaying exponential basis functions. This enforces the contraction requirement stated in condition (23). It is evident from Table-5 that the ROM-HPM solutions rigorously satisfy the sufficient convergence conditions (24) over the entire computational domain. Furthermore, the obtained velocity fields (u, v) strictly satisfy the continuity constraint (25)(i), while the computed pressure gradients $\frac{\partial p}{\partial x}$ and $\frac{\partial p}{\partial y}$ satisfy Euler's compatibility condition (25)(ii). Taken together, these findings confirm the internal consistency and convergence compliance of the proposed approach, thereby reinforcing the credibility and robustness of the ROM-HPM solutions shown in Figs.7-11.

After substituting (λ_1^*, r_1^*), we compute a series based solution and compare it with the CFD solutions in Figs.7-10 for the Newtonian case $(\alpha = 1)$ and in Fig.11 for the non-Newtonian case $(\alpha \neq 1)$. The CFD methodology used in our group [16–19] and described in section-3 are utilised to compute the numerical solutions of equation (56) subject to the boundary conditions (58) with additional outlet boundary as $x = 25 : \frac{\partial u}{\partial x} = 0, \frac{\partial v}{\partial y} = 0$. As seen from Fig.7, our computed axial (u) and radial (v) velocities matches very well with the CFD solution across different channel lengths (x) for case-A. The maximum relative error for u is about 0.23% near the centerline and close to the outlet $(x = 24)$, while for v, the error is around 0.68% near the bottom wall $(y = 0.15)$ and close to the inlet flow $(x = 0.5)$.

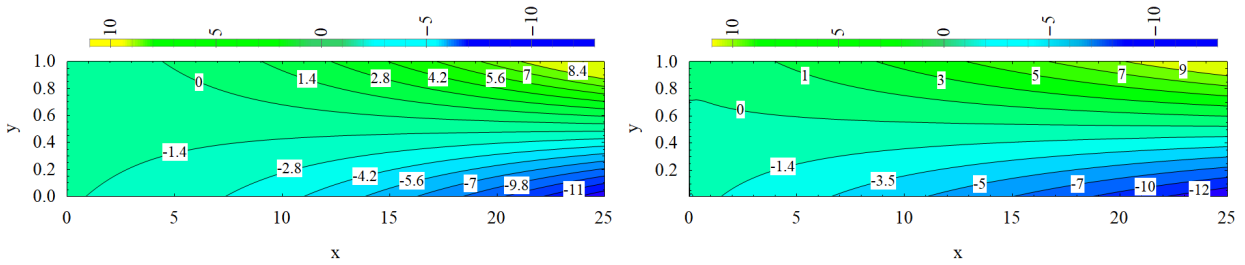
Fig.8 represent the comparison of vorticity contour of the computed ROM-HPM solution (Fig.-8(a)) with CFD solution (Fig.8(b)) for the above case-A. It is clear that our analytical solution matches qualitatively and quantitatively very well with numerical solution. From Fig.8 we see that the injection likely induces a vertical velocity component near the bottom boundary, which interacts with the horizontal flow. This creates shear layers where vorticity develops, especially near the boundary region. That is, the injection modifies the boundary layer dynamics, leading to stronger vorticity gradients near the walls. Therefore, key flow properties, including shear stress, can be effectively analyzed using our ROM-HPM.

Similarly, in Fig.9 we compare the computed axial velocity with those of CFD results at the different x for the case-B and Newtonian case $(\alpha = 1)$. The schematic diagram of top wall variable



(a) (b)

Fig. 7: Comparison of computed semi-analytical velocities with those of CFD solution at different x for the Newtonian case ($\alpha = 1$) subject to constant injection at the bottom wall and no injection/suction at the top wall (case A): (a) axial velocity (u); and (b) radial velocity (v).



(a) (b)

Fig. 8: Comparison of vorticity contours for the Newtonian case ($\alpha = 1$) under case A: (a) semi-analytical solution; and (b) CFD solution.

injection/suction is shown in Fig.9(a). As x increases (from $x = 0.5$ to $x = 24$) the v velocity becomes more negative, indicating a strong injection from the top wall. As seen in Fig.9(b), at all position x, the analytical curves (solid lines) and CFD data points (symbols) overlap well. The results suggests that ROM-HPM effectively captures the boundary layer behavior. Furthermore, in Fig.9(c) we present the solution for the channel length $x > 25$ for this case-B. It may be noted that CFD data beyond $x = 25$ is not available, since CFD computation was based on definite channel length $[0, 25]$. This setup introduces interesting dynamics as the interaction of injection and suction significantly shaping the velocity field at different channel length x. The constant injection at the bottom wall pushes fluid into the domain, resulting in an upward increase in velocity. While, the top wall injects fluid into the domain upto $x = 80$ with maximum injection at $x = 40$ (ref. Fig.9(a)). Therefore, interaction between injection at both walls accelerates the flow, leading to enhance velocity as reflected in Fig.9(c) at $x = 30$ and $x = 40$ (solid line). During $x = 40$ to $x = 80$, intensity at injection decreases and $v_T = 0$ at $x = 80$. When the top wall has suction beyond $x = 80$, fluid is removed from the flow domain (ref. Fig.9(a)). This causes a steeper velocity gradient in the region closer to the top wall, as the suction competes with the bottom wall's injection. At larger x, the effects of combine injection or suction become more pronounced. As a result, velocity start decreasing beyond $x = 40$ and flow becomes minimal at $x = 120$ (ref. Fig.9(c). Finally u velocity becomes negative at $x = 130$ due to strong suction, except very close to the top

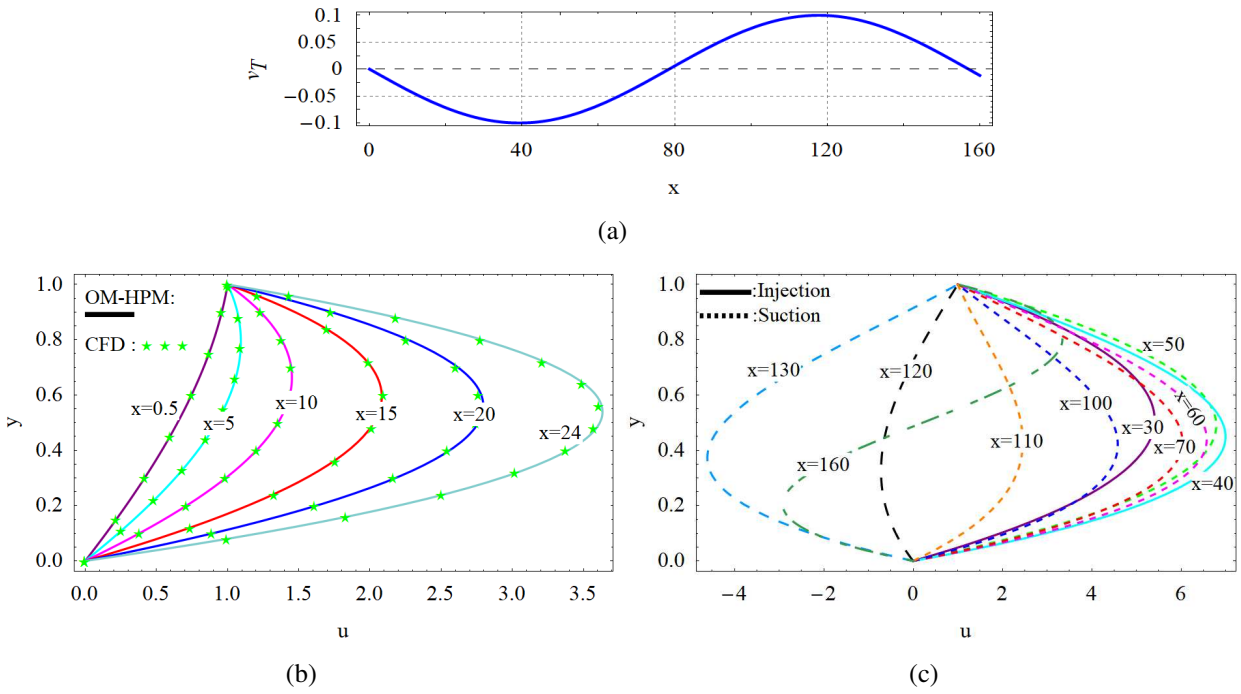


Fig. 9: (a) Schematic representation of the variable injection-suction condition at the top wall (v_T) in case-B of the non-Newtonian flow problem. (b) Comparison of computed semi-analytical axial velocity ($u(x, y)$) with the CFD solution for Case-B and the Newtonian case ($\alpha = 1$) at various x; (c) Extension of the semi-analytical u-velocity to larger x.

wall due to movement of the top wall. At $x = 160$, u velocity becomes both positive and negative. Therefore, physically the problem becomes two dimensional under this flow situation, and our semi-analytical method (ROM-HPM) could able to capture flow characteristics inside the channel, and finally it matches with numeric solution by well established CFD technique upto $x = 24$.

Fig.10 shows the contour plots of the vorticity (ζ) at different channel lengths for the case-B. There is excellent agreement between our CFD and semi-analytical solution in Figs.10(a)-(b). Next we put an effort to extend the channel length beyond $x = 25$ using our analytical expression and presented in Fig.10(c) and 10(d) for $x = 100$ and $x = 175$, respectively. As can be seen here that strength and center of positive and negative vorticities observed in Fig.10(b) are not exactly same in Fig.10(c) for longer channel. This is not surprising, because our analytical solution expression contains the term "$\sin\left(\frac{x}{25}\right)$"due to variable injection-suction from the top wall. Therefore, physically, the problem for Fig.-10(c) is not the same as for Figs.10(a)-(b). When we extend the channel length further upto $x = 175$, we are wondering to observe two opposite sign vorticities on the bottom wall in Fig.10(d). This is due to strong interaction from the bottom wall injection and variable injection-suction from the top wall. That is, vorticities are generated inside the channel without any obstacle (against the flow) with the help variable injection-suction. This was also observed by Mondal and Maiti [16] for other form of v_T where both injection-suction are applied within the channel length upto $x = 25$. Needless to mention that the results of Fig.10(a) by CFD can not be extended to like Fig.10(c) and Fig.10(d), without doing fresh calculation.

Now, we explore the non-Newtonian fluids ($\alpha \neq 1$), characterized by the power-law index α and compare the solutions with the CFD solutions, as shown in Fig.11. Fig.11(a) shows the u velocity along the y-direction at different x-positions for the case-A. The CFD solutions (symbols) closely match with the ROM-HPM's solutions (solid lines) for $\alpha = 0.8$, with maximum relative

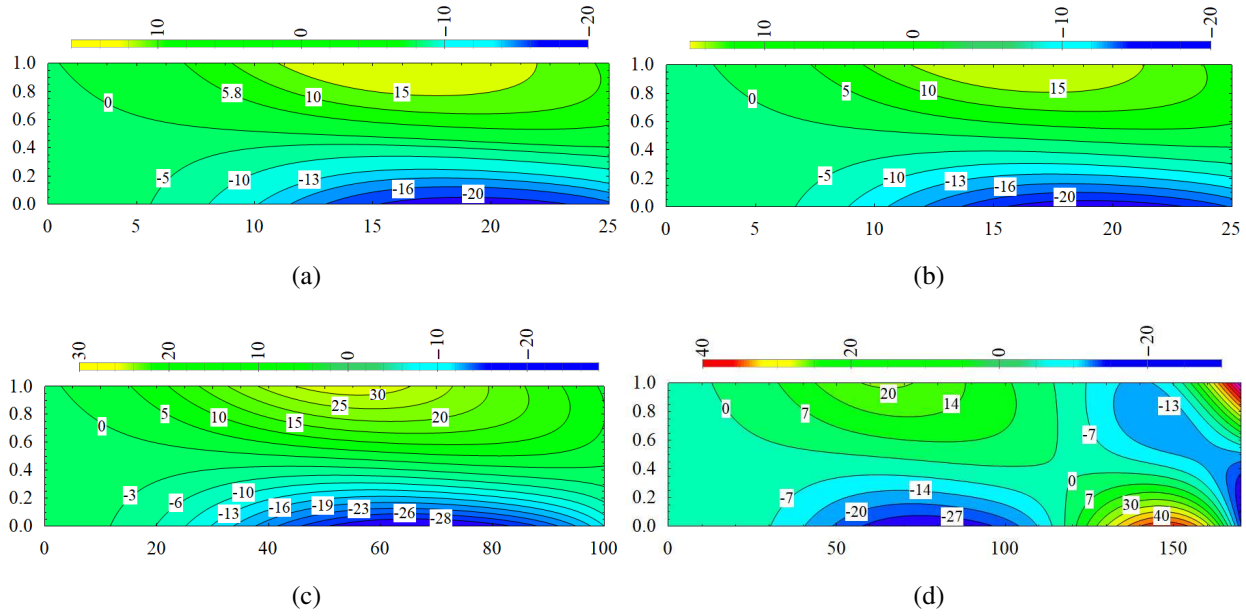


Fig. 10: Vorticity contour for the Newtonian case ($\alpha = 1$) subject to case-B: (a) CFD vorticity, (b)-(d) our semi-analytical vorticity at different channel lengths. Vertical and horizontal direction represents x- and y-axis, respectively.

error of 1.54%. In Fig.11(b), our analytical solutions (solid lines) also agree with the CFD results (circles) with maximum relative error 0.14%. Fig.11(c) compares the u-velocity profiles at different power-law indices $\alpha = 0.5, 1, 1.5$ and different axial positions $x = 5, 10, 15$. From Fig.11(c) we see that our semi-analytical solutions (solid lines) completely agree with the CFD solution (symbols). The Newtonian case serves as a baseline with moderate resistance and uniform behavior. Non-Newtonian fluids show significantly altered velocity profiles due to their shear-dependent viscosity: shear-thinning fluids enhance flow in high-shear regions, while shear-thickening fluids resist flow in the same regions. On the other hand, Fig.11(d) presents a similar comparison for Case-B, showing u velocities at different values of α and x. The semi-analytical solutions are in close agreement with the CFD ones, with a maximum relative error of 1.86% near the centerline and outlet.

Case-C: Time dependent wavy injection-suction on both walls.

We attempt here to explore the possibility of capturing the unsteadiness in the N-S equations by our ROM-HPM. We continue with the same physical geometry, i.e., micro-channel with variable injection-suction. For which we consider the following time-dependent variable injection-suction from Mondal and Maiti [16] as

$$v_T = 0.1 \sin\left(\frac{x}{2.5}\right) \text{ and } v_B = 0.1 \sin x \cos\left(0.4\Pi x\right) \cos\left(2\Pi t\right) \tag{62}$$

The wavy injection-suction mechanism have diverse applications in scientific and technical problems, such as cooling system, boundary layer control, drag and flow separation. Fig.12(a) presents the schematic diagram of the physical problem in the form of v_T and v_B. In Fig.12(a), the top and bottom walls show sinusoidal waves, indicating the periodic nature of the injection-suction process. Injection/suction is fixed at any point on the top wall; however, on the bottom wall it varies with x and t. That is, at a fixed point on the bottom wall, the amount of fluid (injected or sucked) is dependent on time periodically with period 1 and amplitude $0.1\sin(x)\cos(0.4\pi x)$, (ref. Figs.12(b)-12(c)). From 12(c), how the amplitude $0.1\sin(x)\cos(0.4\pi x)$ depends on x is clear. Moreover, the

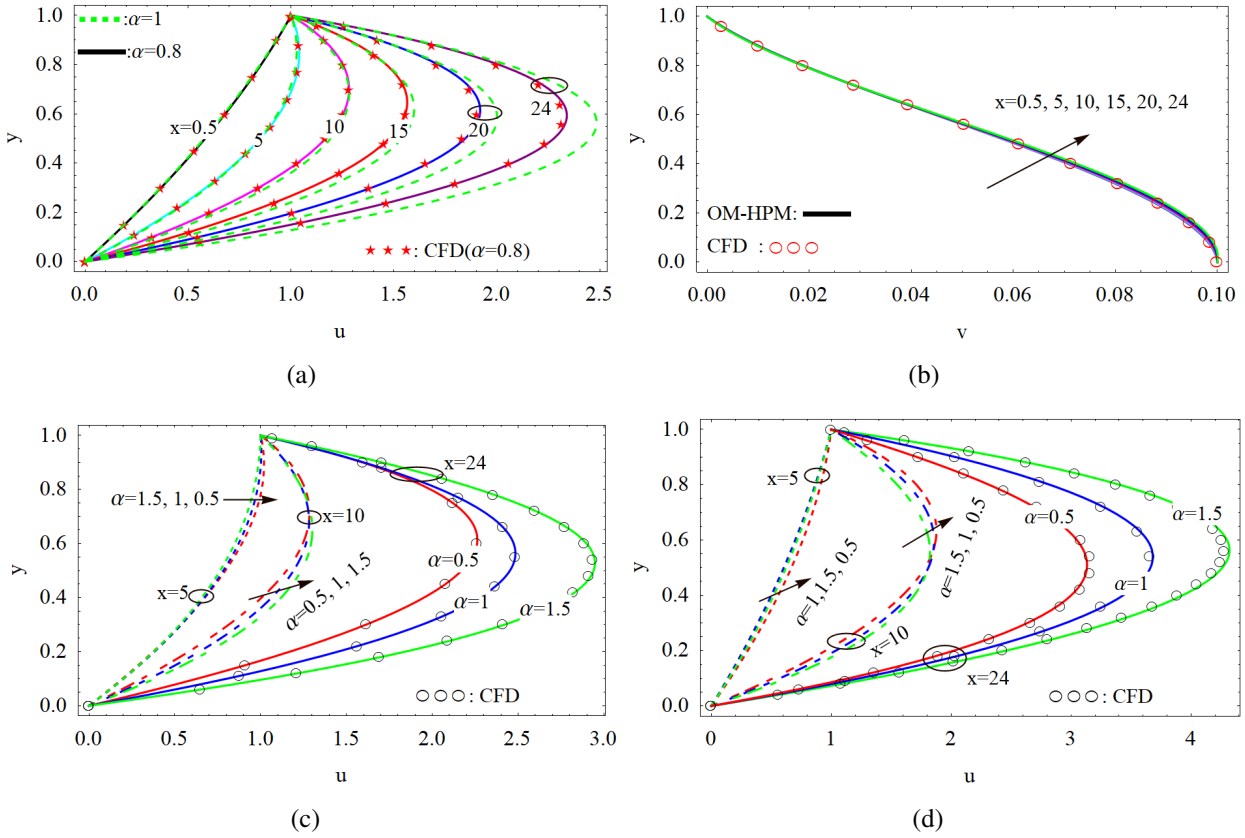


Fig. 11: Comparison of computed semi-analytical velocities with those of CFD solution [16] for the non-Newtonian case: (a) axial velocity (u) at different x with fixed $\alpha = 0.8$ for case-A, (b) radial velocity (v) at different x with fixed $\alpha = 0.8$ for case-A, (c) axial velocity (u) at different $\alpha = 0.5, 1, 1.5$ and $x = 5, 10, 24$ for case-A, and (d) axial velocity (u) at different $\alpha = 0.5, 1, 1.5$ and $x = 5, 10, 24$ for case-B.

amplitude function $0.1\sin(x)\cos(0.4\pi x)$ is a periodic function with period 8π $(= 25.13)$. Therefore, we introduce a chaotic unsteadiness in the boundary condition.

Analogous to Table-5, Table-6 summarizes the convergence behaviour of the ROM-HPM for Case C (62). The results indicate that the minimum residual Δ_1 is already sufficiently small at the lowest approximation order ($m = 1$) to satisfy the basic OM-HPM convergence requirement, whereas the pressure-dependent ROM-HPM formulation necessitates slightly higher-order terms. By the fifth-order approximation, the solution also fulfills the additional convergence criterion (25) within a tolerance of 10^{-6}. As in Table-5, the optimal convergence-control parameters assume negative values, thereby ensuring compliance with the contraction condition (23). We also compare the CPU-time for the ROM-HPM in the same table and seen that to achieves desire accuracy, ROM-HPM requires 16 minutes, whereas CFD techniques require an average of about 50 minutes for each parameter set.

Fig.13 shows variation of velocities (u, v) with time along with their corresponding spectra at different positions inside the channel (x, y). It is clear that our solution of non-linear N-S equations becomes dependent on x, y, and t. Both velocity components oscillate periodically with the period introduced at the boundary condition. However, amplitude of oscillation increases as we move towards the end of channel (ref. spectra in Fig.13). The enhancement of amplitude is more for the vertical velocity (v). Moreover, the amplitude of spectra of v is seen more when v is chosen very close to the bottom wall, because the fluid flow is largely affected at this area.

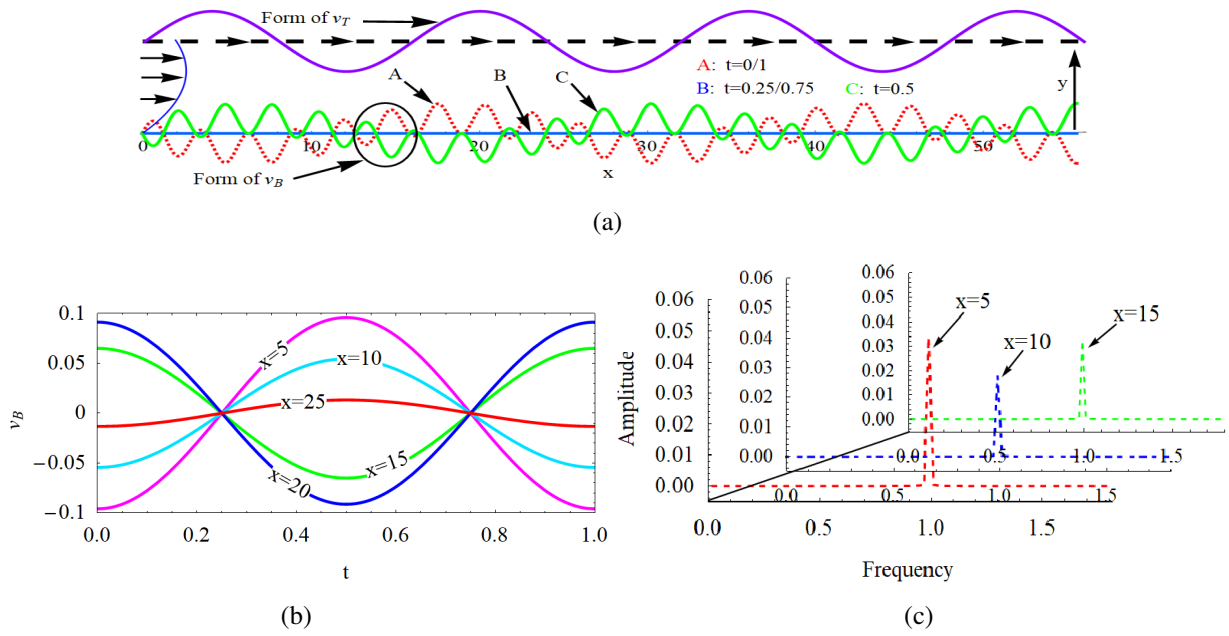


Fig. 12: (a) Schematic diagram of flow configuration for case-C of non-Newtonian problem; (b) Bottom wall injection-suction (v_B) as a function of t within $[0, 1]$ at different axial position x; and (c) Corresponding spectra of the time signals in (b) at various x over $t \in [0, 1]$.

Table 6: Convergence test for Case-C ((62)) along with CPU usage for different orders of approximation (m) and a fixed parameter set $Re_u = Re_v = 1.24, P = 0.1, \alpha = 1$.

m	(λ_1^*, r_i^*)	Δ_m	Additional Condition (25)		CPU time
			Condition-i	Condition-ii	(min)
1	$-5.41339,\ -3.72968$	2.33×10^{-9}	6.43×10^{-3}	7.72×10^{-3}	0.8
3	$-2.69092,\ -1.73365$	1.97×10^{-11}	3.71×10^{-4}	6.53×10^{-4}	3.1
5	$-1.54252,\ -1.15834$	1.17×10^{-14}	1.02×10^{-6}	1.04×10^{-6}	16.4

Fig.14(a) presents the variation of axial velocity $u(x, 0.5, t)$ along center line ($y = 0.5$) at $t = 0$ and 0.5. At the entrance of the channel, u-velocity is small and starts oscillating within $(0, 1)$ for $x > 5$, and then as we move beyond the entrance, the magnitude of velocity increases as well as amplitude of oscillation with respect to x gradually increases upto $x = 30$, and then both drastically increases, then finally unpredictable at both $t = 0$ and 0.5. Nevertheless the period of fluctuation is remain same at both times,resulting to same frequency and amplitude of fluctuation u at both times $t = 0$ and $t = 0.5$ (ref. spectra inside Fig.13(a)). The curve of fluctuation at $t = 0$ is complementary to that at $t = 0.5$ since the boundary condition at $t = 0$ and 0.5 are opposite to each other. That is, our propose method have correctly capture the input value. Similarly if we see in Fig.14(b), the variation of u along x at a fixed time $t = 0.25$ around bottom ($y = 0.25$), center ($y = 0.5$) and top ($y = 0.75$), u-velocity changes chaotically as x increases. This is confirmed from the spectra of fluctuation with multiple peaks at these points inside Fig.14(b). The amplitude of fluctuation is maximum at the channel center. Eventually, the frequency remains the same at all y value. Similar attempt is made for the vertical velocity in Fig.14(c). Radial (v)-velocity at these three positions

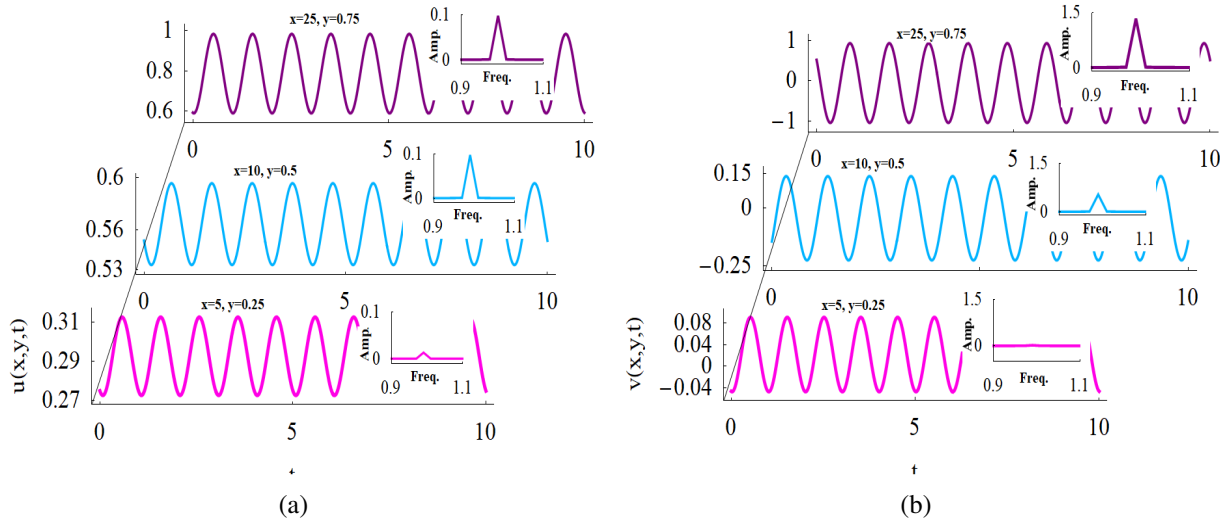


Fig. 13: Velocity as a function of time t at different positions (x, y) in the channel, with corresponding spectra shown within each subfigure: (a) Axial velocity (u); and (b) Radial velocity (v).

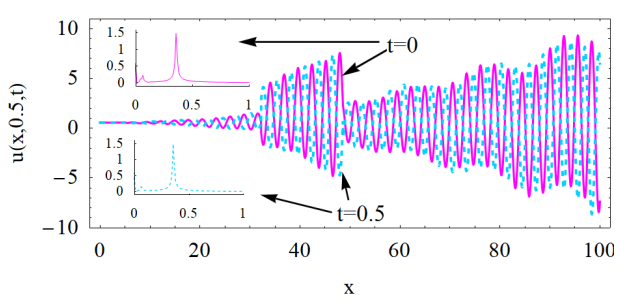
$(y = 0.25, 0.5, 0.75)$ changes sinusoidally with same period, which can be confirmed from the spectra. Here, the radial velocity fluctuation is uniform in comparison to that of axial velocity. Here also maximum fluctuation is occurred at center of the channel. Dominant peak of spectra of u-velocity (ref. Fig.14(b)) falls at the same position in the spectra of v-velocity in Fig.14(c). It is to note that v-velocity increases drastically as x increases.

To further illustrate the fluid motion over time and space, we present the vorticity contour on the region $x \in [15, 25]$ at ten different times in one period $t \in [0, 1]$ in Fig.15. A developed flow (alternative positive and negative vortices) is observed after certain channel length x ($x > 10$) (ref. Fig.15). At a glance, vorticity contour during a period shows how the flow is influenced by varying rates of injection and suction, leading to the development of coherent structures in the flow. There are

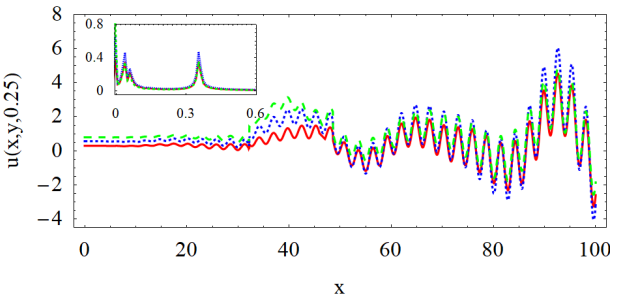
- Elongated (positive/negative) vortices (ref. Figs.15(a)-(b),15(f), 15(j)).
- Partially developed vortices (at top/bottom wall with positive/negative vortices (ref. Figs. 15(c)-(d),15(g)-(h)).
- Fully developed vortices (positive/negative vortices occupying fully between and bottom walls (ref. Figs.15(e), 15(i)).

In other words, sign of vortices depends on whether there is maximum injection/suction, or transition between injection and suction. This confirm that these vortices are not rolling as like as Karman vortices.

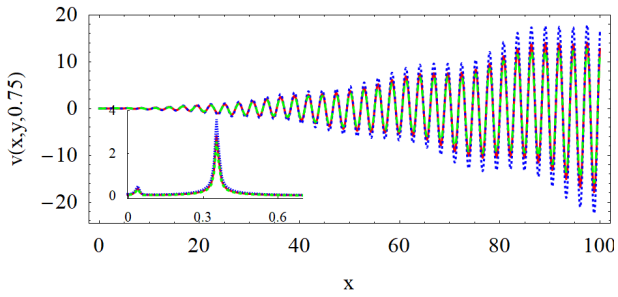
In order to discuss the flow development during this period, we take a particular region ($20.5 < x < 21.5$ of the channel). As seen in Fig.15(a) an elongated negative vortex (with maximum strength towards the bottom) is observed at $t = 0$ at which there is maximum injection (ref. Fig.16, form of v_B). Apparently, flow features at $t = 0$ and $t = 1$ are exactly the same (ref. Figs.15(a),(j)). As time progress, injection decrease (ref. form of v_B in Fig.16), the flow starts to respond to the rate of injection and then negative vortex strength diminishes (Fig.15(b) at $t = 0.05$). At $t = 0.1$ (ref. Fig.15(c)) the elongated vortex initiate to break, while a partially developed positive vortex



(a) Axial at $y = 0.5$ and different t



(b) Axial at $t = 0.25$ and different y



(c) Radial $t = 0.25$ and different y

Fig. 14: Computed velocity profiles at different times and spatial positions in the channel, with corresponding spectra shown within each panel: (a) Axial velocity along the centerline ($y = 0.5$) at $t = 0$ and $t = 0.5$; (b) axial velocity at fixed time $t = 0.25$ along transverse positions $y = 0.25, 0.5$, and 0.75; and (c) radial velocity v at $t = 0.25$ along the same transverse positions as in (b).

originated from the top wall around $x = 20$ is trying to dominate over the aforesaid negative vortex at the bottom wall. Thereafter, at $t = 0.25$ (ref. Fig.15(d)) when there is no injection or suction from the bottom wall, the dominant positive vortex becomes larger and more pronounced. As time progress the vorticity contours not only change in shape but also its intensity. Finally at $t = 0.35$ (when the bottom wall starts to suck the fluid, ref. Fig.16, form of v_B) the above positive vortex takes its complete form occupying from top to bottom around $x = 20$ (ref. Fig.15(e)). Peaks in the vorticity indicate regions of high rotational motion , which can affect mixing and energy transfer within the fluid. For further increase of suction at the bottom wall, as seen in Fig.15(f) at $t = 0.5$ at which there is maximum suction (ref. Fig.16, form of v_B), the well defined positive vortex changes its shape to an elongated vortex with maximum strength towards the bottom wall. This elongated vortex is similar to that at $t = 0$, but sign of rotation is completely opposite. This is not surprising, because periodic form of v_B ((ref. Fig.16) with period 1 gives opposite flow situations at $t = 0$ and $t = 0.5$. Owing to this periodic boundary condition, a flow development during $[0.5, 0.85]$ (elongated positive vortex at $t = 0.5$ to well defined negative vortex at $t = 0.5 + 0.35$) is eventually similar to that during $[0, 0.35]$, but rotation of vortices are opposite to the previous one. One may confirm this argument by comparing the coherent structure of vortices between $t = 0.25 \in [0, 0.35]$ and $t = 0.75 \in [0.5, 0.85]$. Because, at the bottom wall flow condition during $[0.5, 0.85]$ (changing injection to suction) is opposite to that during $[0., 0.35]$ (changing suction to injection) (ref. form of v_B in Fig.16).

In order to summarize this discussion on the formulation and development process of vortices on the domain $x \in (20, 21)$, we present Fig.16 where we have schematically shown the vortices during a period $[0, 1]$. Here curve solid line present the form of injection-suction (v_B) at the bottom

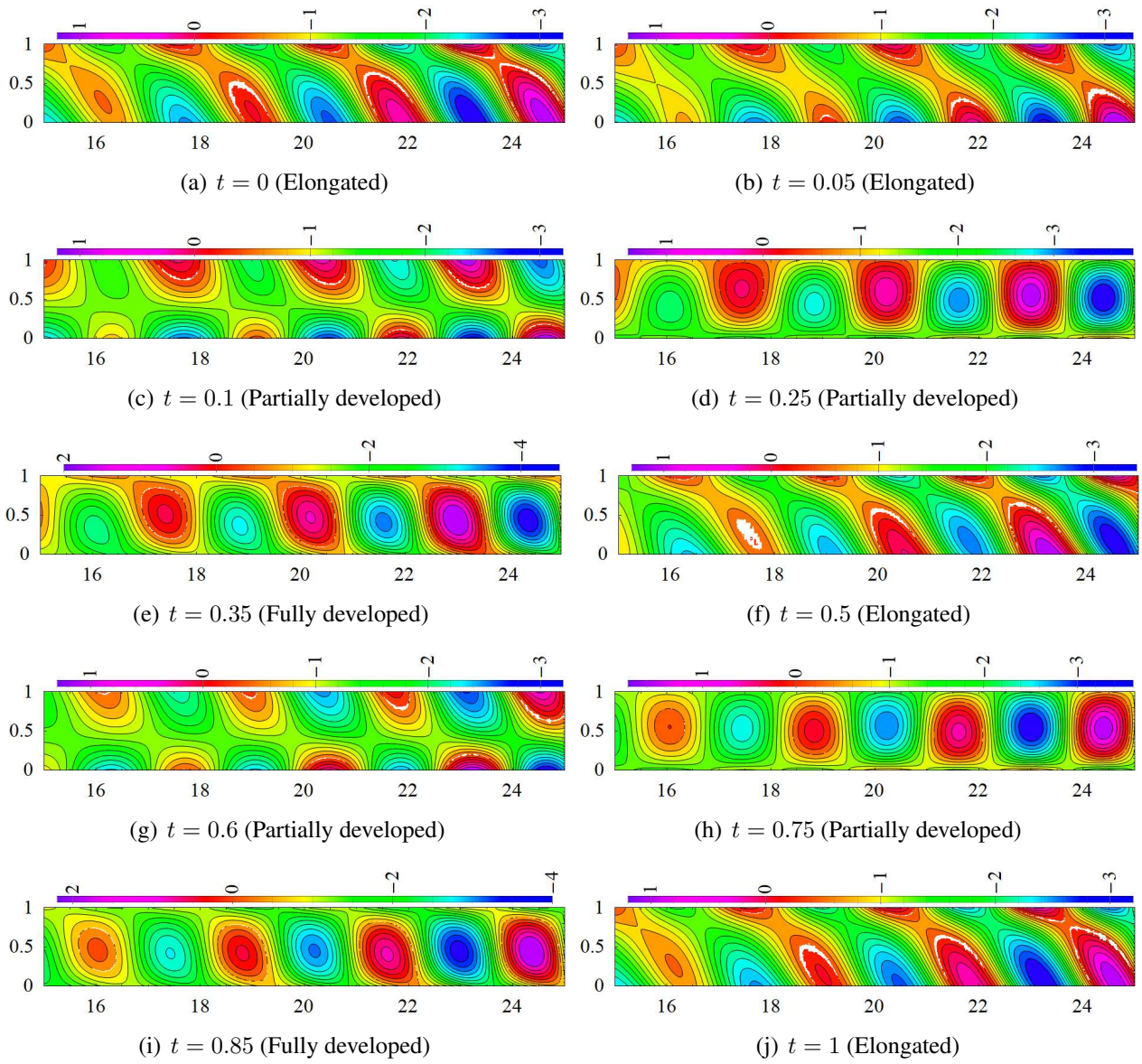


Fig. 15: Vorticity contours for the Newtonian case ($\alpha = 1$) at different times instants within one period $t \in [0, 1]$, illustrating the evolution of vortices: elongated, partially developed, and fully developed structures. Vertical and horizontal directions represent y- and x- axes, respectively.

wall in a period $[0, 1]$. From this figure it may be conclude that

- A vortex becomes elongated at a time when there is maximum injection (producing negative vortex) or suction (producing positive vortex),
- A vortex becomes partially developed at the top wall when there is transition from injection to suction (producing positive vortex) or suction to injection (producing negative vortex), and
- A vortex becomes fully developed when there is increasing suction (leading to positive vortex) or injection (leading to negative vortex).

The aforesaid formation and development process of vortex on the region $x \in (20, 21)$ during a period is to be applied in any other region $x > 10$. But only the differences are the strength and sign

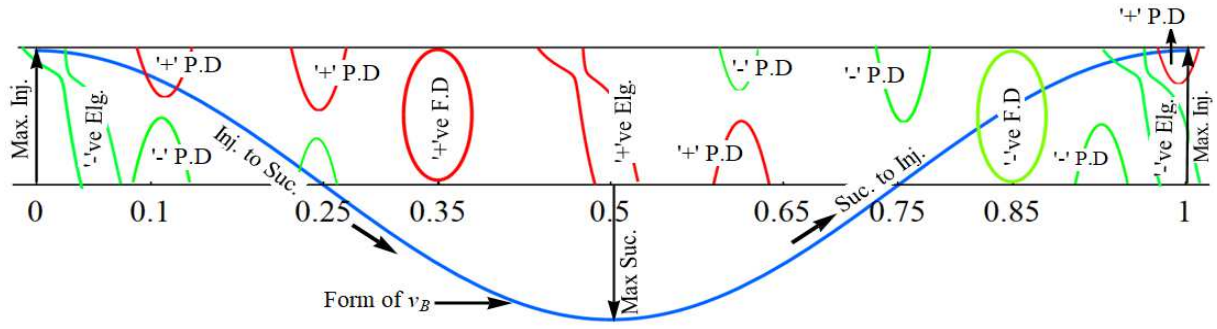


Fig. 16: Schematic diagram showing the development of vortical structures: elongated (Elg.), partially developed (P.D.), and fully developed (F.D.) over one period $[0, 1]$ in the region $x \in (20, 21)$. The solid blue curve represents the time variation of bottom-wall injection (Inj.) and suction (Suc.) velocity, v_B, at $x = 20$. The annotated values along the bottom wall indicate the corresponding time instants $t \in [0, 1]$.

of the rotation, which depends on the rate of injection-suction $(0.1 \sin(x) \cos(0.4\pi x))$. For this we have presented Fig.17, where Fig.17(f) presents the form of v_B in $[0, 1]$ at $x = 20$ and $x = 30$. The injection-suction at $x = 30$ is exactly opposite to that at $x = 20$ for any time. Therefore, at any time, we should have a vortex near $x = 30$ with sign opposite to that near $x = 20$. For example, at $t = 0$ and $t = 0.5$, we see that there is elongated positive (ref. Fig.17(b)) and negative (ref. Fig.17(a)) vortices, respectively, near $x = 30$. This also confirms our ongoing arguments to have an elongated positive (negative) vortex at a time $t = 0$ ($t = 0.5$) when there is maximum suction (injection) in Fig.17(f). As can be seen in Figs.17(b) and (d), number of vortices in any range of x are same at $t = 0$ and 0.5, but arrangement of vortices is opposite to each other (positive to negative, or vice versa). From Fig.17(e), it is clear that as channel length increases strength of vortices also increases.

Therefore, the obtained results convincingly validate the underlying physical mechanisms of the problem and strongly reinforce the reliability and robustness of the solutions generated by the ROM-HPM.

4.2.2.3 ROM-HPM versus CFD (Continuous and Discrete): A Comprehensive Methodological Review

Now we attempt to compare two solutions of ROM-HPM: (i) **Continuous situation:** which is obtained by substituting the particular value of t in the obtained general solutions in terms of x, y and t, (ii) **Discrete situation:** which is obtained freshly based on the B.C after putting the particular t value in v_B. That is, first one is the unsteady solution and we are indeed to see the flow at any instant, while the second one is the steady state solution, similar to case-A and case-B. We present the vorticity contour for the second case in Fig.18(a) (at $t = 0$), Fig.18(b) (at $t = 0.25$) and Fig.18(c) (at $t = 0.5$) and compare with their counter part in continuous situation presented in Figs. 15(a), 15(d) and 15(f), respectively. We see that two solutions (continuous and discrete) match each other at a time ($t = 0$ and 0.5) where there is either maximum injection or suction from the bottom wall (ref.: $t = 0$ (Figs.15(a) and 18(a)), $t = 0.5$ (Figs.15(f) and 18(c))). However, it is to note that Figs.15(d) and 18(b) are not identical at $t = 0.25$ (and $t = 0.75$) at which $v_B = 0$. Under discrete situation the solution is computed based on v_B (no injection-suction from the bottom wall) at $t = 0.25$ and the flow is mostly dominated by the top wall injection-suction. On the other hand, the flow inside the channel during a period $[0, 1]$ in Fig.15, there is a continuous flow development process in the sequence: elongated, partially and fully developed. The vorticity contour in Fig.15(d)

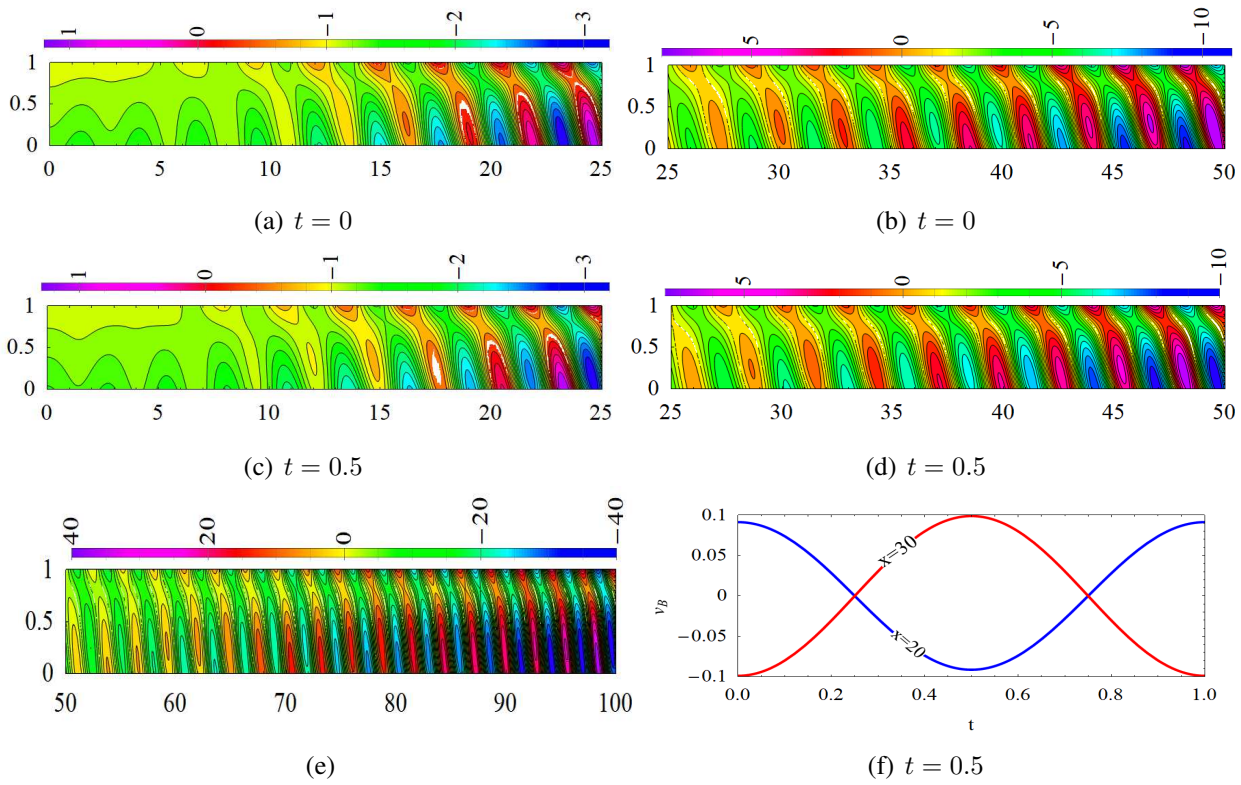
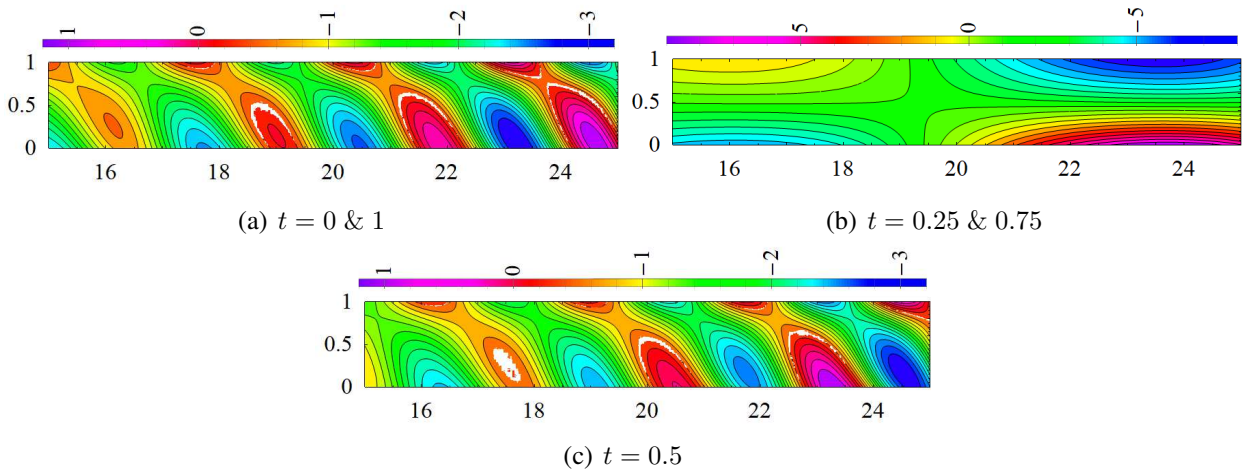


Fig. 17: Vorticity contours at different time and domain extents: (a, b) at $t = 0$ in a small domain ($x \in [0, 25]$) and a large domain ($x \in [25, 50]$), respectively; (c, d) at $t = 0.5$ in the same respective domains; (e) at $t = 0$ in a very large domain; (f) wavy bottom-wall velocity, v_B, as a function of time at $x = 20$ and $x = 30$.

is the flow feature at an instantaneous time $t = 0.25$, which falls in the aforesaid period, at which there is partially developed vortices. Therefore, ROM-HPM solution in terms of t (unsteady) is physically realistic. At the points of maximum injection or suction, the continuous and discrete cases show minimal differences due to the stability in the flow (see Figs. 15(a), 18(a), 15(f), and 18(c)). However, during the transition phase between injection and suction, noticeable differences arise as the continuous momentum acts like an acceleration, causing instability in the flow.

Now we attempt to compare our ROM-HPM solution with those of CFD solution by Mondal and Maiti [16] at discrete time, for which we present Fig.19. Vorticity contours in Figs.19(a) and 19(b) are respectively, closer view of Figs. 8(e) and 8(i) of Mondal and Maiti [16]. It is to note that the computational procedure (CFD discrete) is analogous to ROM-HPM discrete. In CFD discrete, solution is computed at a discrete time subjected to the boundary condition at the specified time. As can be seen, Fig.19(b) matches with Fig.18(b) at $t = 0.25$ (or 0.75) at which $v_B(x) = 0$. This is similar to Case-B. However, at other times t at which $v_B(x) \neq 0$ and wavy, CFD result do not match with the discrete-time-based ROM-HPM solutions (ref. Figs.18(a) and 19(a) at $t = 0$ or 1). Figs.19(c) and 19(d) present vorticity contours of ROM-HPM and CFD solutions, respectively, for the case of same $v_T(x)$ as Case-C, but constant $v_B(x) = 0.1$. As can be seen here, CFD solution again fails to match with that of ROM-HPM. Next we put effort to extend the situation of Figs.19(c) and 19(d) by increasing the number of wavy oscillation in $v_T(x)$ $(= 0.1 \sin\left(\frac{x}{1.25}\right))$ but $v_B(x) = 0$ and presented in Figs.19(e) and 19(f). Apparently they do not match. It may be deduced that for the cases of (i) both $v_T(x)$ and $v_B(x)$ are non-zero and any one of them is wavy, and (ii) any one of them is zero and other one have more periodicity, CFD solution fail to achieve the ROM-HPM



(a) $t = 0$ & 1 (b) $t = 0.25$ & 0.75

(c) $t = 0.5$

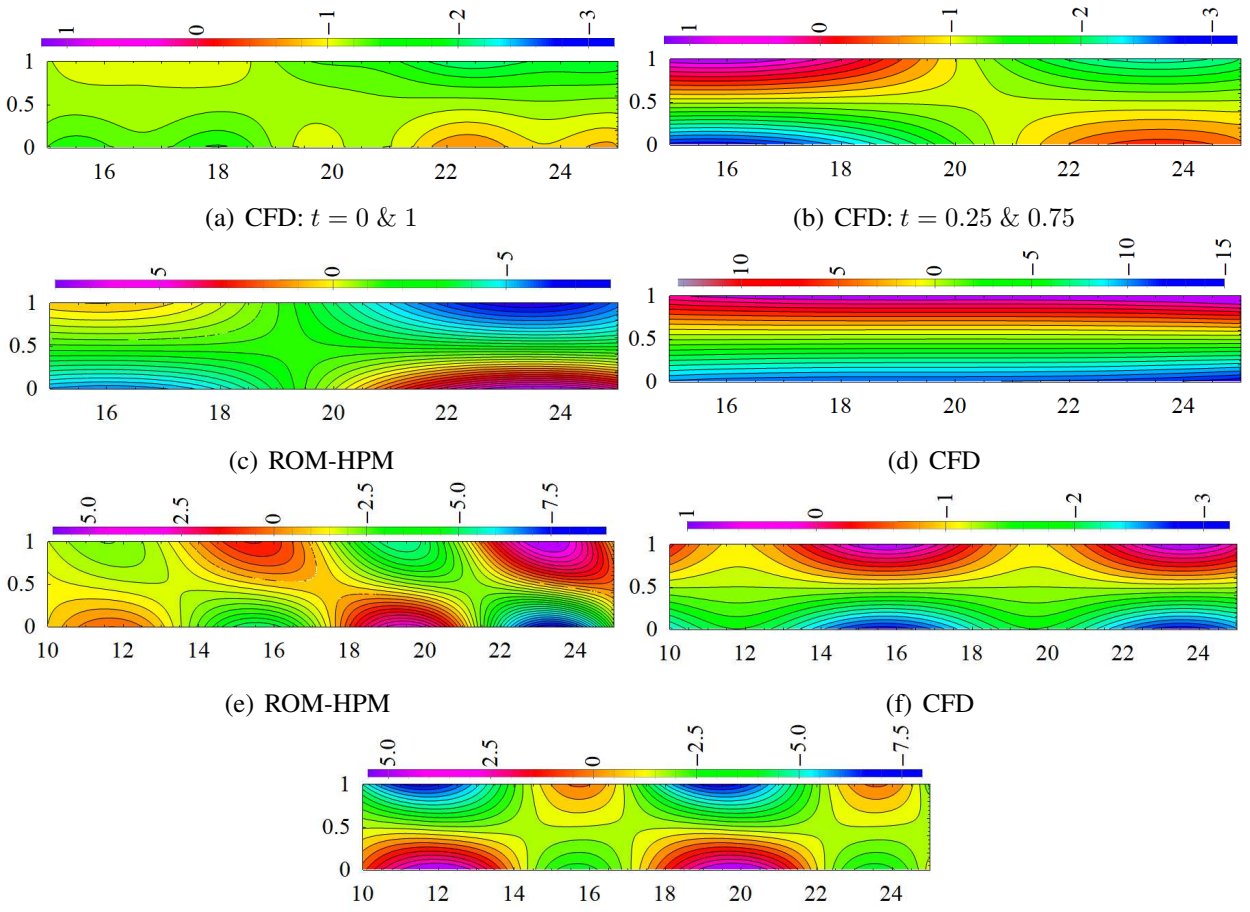
Fig. 18: Vorticity contours at selected time instants over one period $t \in [0, 1]$, obtained using the proposed ROM-HPM (Discrete) formulation. The wall velocity v_B is prescribed by discrete substitution of t values prior to solution evaluation.

solution.

Subsequently, the CFD solutions are presented in Fig.19(g) by increasing the amplitude in the wavy form of $v_T(x)$ $(= 0.6 \sin\left(\frac{x}{1.25}\right))$. Now, we see Fig.19(g) approaches to Fig.19(c). Therefore, in order to achieve solution of ROM-HPM in Fig.19(e), one has to increase the amplitude of oscillation in the periodic form of $v_T(x)$ (ref. Fig.19(g)). Such disorder of CFD could be due to deficiency of transmission of boundary information towards the flow domain. In CFD, the fluid domain is divided into finite number of control volume in order to discretize the governing equation using FVM. So boundary condition at both permeable walls in CFD are specified at discrete points, in contrast to use of continuous boundary condition in its counter part ROM-HPM. Therefore, the bulk flow rate across the wall in CFD is expected to be less than that of ROM-HPM (ref. Figs.19(e)-(g)).

Now we aim to compute CFD continuous solution, which is time dependent, similar to ROM-HPM continuous solution (ref. Figs. 13-17). CFD solution is computed at each time step t_n using the previous time step solution at t_{n-1} as initial guess along with the boundary condition at $t = t_n$. Then the solution is advance in time based on $t_{n+1} = t_n + n\triangle t$, $n > 0$. Initially, $\triangle t$ is considered as 10^{-6} and then as time progress $\triangle t$ increase subsequently and finally it is set to 10^{-5}. We applied this solution procedure for the case-C (ref. Eq.(62)). However, it is observed that, not presented here for the shake of brevity, solution at any time do not match with those of ROM-HPM except at $t = 0.25$ and 0.75, similar to CFD discrete situation. That is, CFD fails to capture the continuous time evolution in this case. Needless to mention that the numerical code described in section-3 used in our previous study [16–19] has been considered here.

Next, we apply our method to a simple case where the discrete results of both ROM-HPM and CFD show good agreement (not presented here). In particular, we consider the bottom wall as $v_B(x) = 0$ and the top wall velocity as $v_T(x, t) = 0.1 \sin\left(\frac{x}{5}\right) \cos(2\pi t)$. This velocity profile exhibits less than one full periodic oscillation within the domain $[0, 25]$, in contrast to the random oscillations observed in case-C. Fig.20 presents the continuous CFD solutions, showing the u-velocity profile as a function of time t, along with the corresponding vorticity contours at selected time instances within the half-period $t \in [0, 0.5]$. Fig.20(a) shows that the u-velocity exhibits periodic oscillations with a period of 1, consistent with the prescribed boundary conditions. We closely examined the flow evolution throughout the period and, for brevity, present vorticity contours only over the half-



(a) CFD: $t = 0$ & 1

(b) CFD: $t = 0.25$ & 0.75

(c) ROM-HPM

(d) CFD

(e) ROM-HPM

(f) CFD

(g) CFD at higher amplitude

Fig. 19: Vorticity contours for different flow situations. (a, b) CFD results for case C at $t = 0$ (or $t = 1$) and $t = 0.25$ (or $t = 0.75$); (c, d) comparison between ROM-HPM and CFD for top wall velocity $v_T = 0.1\sin(x/2.5)$ and bottom wall injection $v_B = 0.1$; (e, f) comparison between ROM-HPM and CFD for the same v_T but with $v_B = 0$; (g) CFD result for the same v_B but with increased top wall amplitude $v_T = 0.6\sin(x/2.5)$, corresponding to the configuration in (e, f).

period. As shown in Figs.20(b)-(f), momentum changes accumulate continuously over time, similar to the flow evolution observed in case-C using the ROM-HPM continuous approach (see Figs. 15-17). This implies that the velocity variation at any time contributes to both the present and future states of the flow in a continuous and interconnected manner. Unlike case-C, where the flow evolves through elongated, partially, and fully developed stages, the current case shows partially and fully developed vortices at $t = 0$ or $t = 0.5$ (maximum injection/suction) and at $t = 0.2$ or $t = 0.225$ (transition between injection and suction), respectively. At $t = 0.25$, where $v_T(x) = v_B(x) = 0$ (the classical C-P flow condition), we still observe the effect of continuous momentum change. Thus, CFD produces realistic and reliable results for simple flow configurations with relatively straightforward boundary conditions. However, as the problem complexity increases as in case-C, where boundary conditions are more complex, one or both porous walls exhibit chaotic or highly wavy structures, the accuracy of CFD solutions tends to loosing and may even produce results that significantly deviate from physical reality. This limitation arises because a truly continuous solution is not possible in CFD due to the inherent discretization of the governing equations and unavoidable

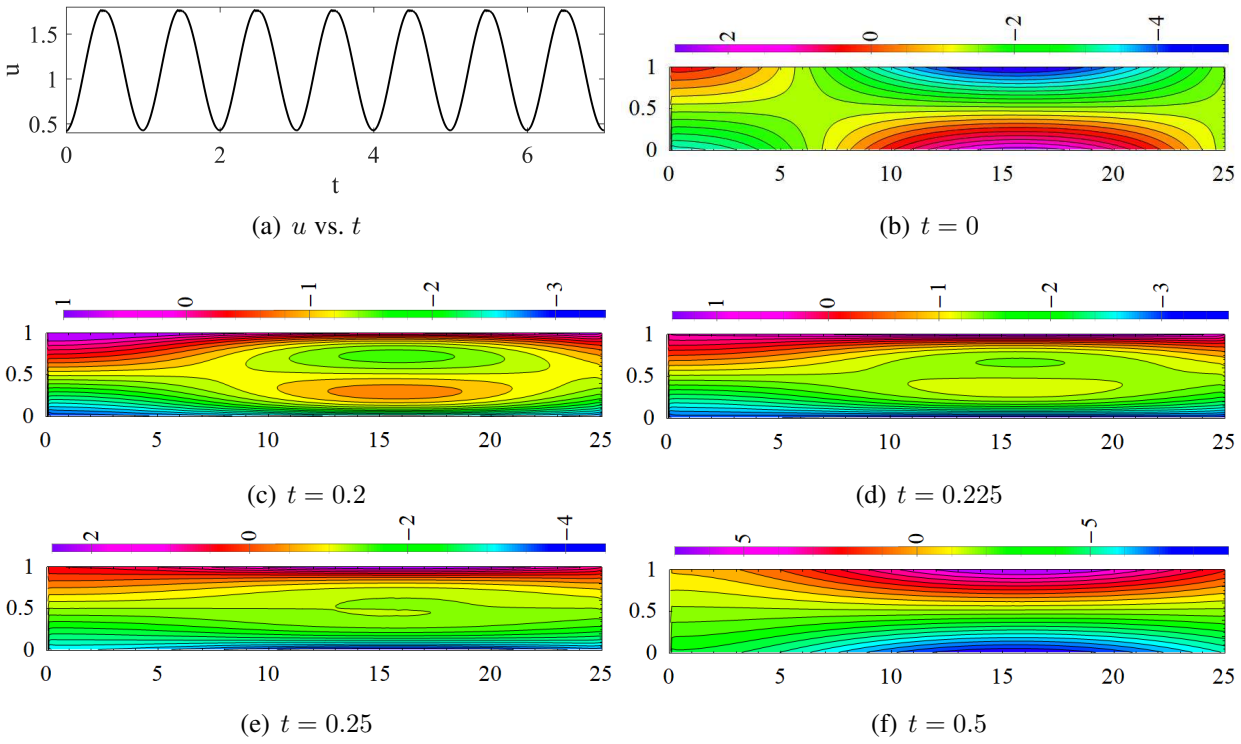


Fig. 20: CFD-based solutions: (a) temporal evolution of axial velocity, while (b)-(f) vorticity contours at different times within one period, $t \in [0, 1]$.

numerical errors.

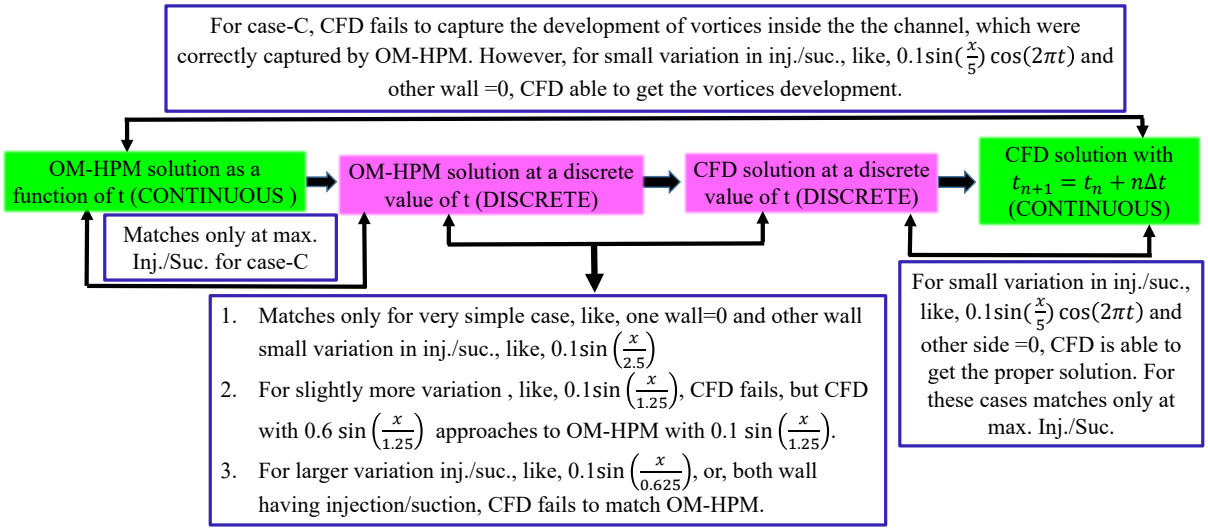


Fig. 21: Summary of key observations from the comparative analysis of ROM-HPM (continuous and discrete) and CFD (discrete and continuous) solutions for case-C: $v_T = 0.1\sin\left(\frac{x}{2.5}\right)$ and $v_B = 0.1\sin x\cos(0.4\Pi x)\cos(2\Pi t)$.

Finally, we summarize the comparison among the result of ROM-HPM (Continuous), ROM-HPM (Discrete), CFD (Discrete) and CFD (Continuous) in Fig.21. Apart from these comparison, it may be noted that grid based CFD tools requires high computational resources and are time consuming. For example, CFD (Continuous) takes approximately 90 hours (i.e. 4 days) for domain

size $[0, 25]$ for time upto $t = 2$, and if we want solution for domain size more than $x > 25$, like, Figs.9(c), 10(c)-(d), 14, 17(b), 17(d)-(e), one has to freshly construct the grid and run the numerical code again. In this exercise the number of grid is expected to be large for a reasonable finer grid solution. Moreover, in channel-type flows with unbounded outlet domains, traditional CFD approaches require truncating the domain to a finite length, which may introduce artificial effects unless carefully treated. In contrast, our proposed method provides a general analytical solution in terms of x, y, t within just few minutes (5-8 minutes) which is valid for the entire semi-infinite domain $x > 0$. Without need of outlet boundary conditions, our explicit analytical solution enables analysis of the flow behavior throughout the entire channel ($x > 0$). Therefore, especially for physical problem with open outlets and variable boundary conditions our semi-analytical method (ROM-HPM) is much more effective and compatible with the physics of the problem, offering a faster and more accurate solution for capturing vortex structures and their evolution in time-dependent flows. Moreover, the proposed ROM-HPM accurately captures nonlinear flow effects and localized vortical structures in unsteady flows with significantly reducing computational overhead compared to conventional CFD.

5. Conclusion and Future Directions

The key findings and insights derived from this study are summarized below:

1. *Summary of Method Development:* we have developed a semi-analytical framework base Optimal Modified Homotopy Perturbation Method (OM-HPM) to directly solve PDE including the full two-dimensional (2D) incompressible Navier-Stokes equations (INSE) without converting to ODE or any simplifications. The general and optimal mathematical strategy for selecting suitable auxiliary linear operators $\mathcal{L}$ and initial approximations u_0 of OM-HPM is extended to PDE. Arbitrary functions within the auxiliary solution framework for PDEs were approximated using polynomials with unknown coefficients, which are systematically determined using the initial and boundary conditions (I.C/B.C). To address the limitations of the standard OM-HPM in handling pressure-driven incompressible flows, an additional algorithm is embedded in OM-HPM, renaming as Refined OM-HPM (ROM-HPM) to accurately compute the pressure field.
2. *Functional Approximation:* Finding arbitrary functions within PDE the polynomial-based approximation of arbitrary functions, compared to the exact form approach, offer greater flexibility and wider applicability, particularly in scenarios with insufficient or surplus boundary conditions.
3. *Convergence, stability, and computational efficiency:* Following our previous theoretical investigation, the present study demonstrates the error bounds, scaling complexity, truncation behavior, convergence, and stability characteristics of OM-HPM and hence ROM-HPM. Both theoretical and numerical analyses confirm that the high stability of our methods arises from the optimal selection of the auxiliary roots λ_i's and hence optimal $\mathcal{L}$, which ensures global convergence. Moreover, OM-HPM/ROM-HPM produces exponentially decaying base function. This significantly reduces scaling complexity and truncation errors at lower orders of approximation, and hence OM-HPM/ROM-HPM becomes computationally efficient.
4. *Pressure Calculation:* We compute the pressure gradients analytically using the proposed homotopy residual-based pressure correction algorithm derived from the momentum equations, analogous to a multi-step method. This formula inherently contains continuity and momentum equations of INSE.
5. *Numerical Validation and Physical Insights:* Initially semi-analytical experiments of OM-HPM on general PDEs, and then extensive semi-analytical and numerical CFD techniques were conducted on Newtonian and non-Newtonian fluid models, with and without pressure terms, in

microchannels featuring porous and slippery walls. It successfully reproduced the exact Couette-Poiseuille (C–P) flow profile without any assumptions, confirming its capability to handle full nonlinearity in the INSE and suppress nonlinear effects when physically insignificant. It has been demonstrated that it can accurately solve unsteady flow features under time-dependent boundary conditions, including the formation and evolution of coherent vortices: elongated (during peak injection/suction), partially developed (during transition phases), and fully developed vortex. These vortex structures are physically consistent and distinctly different from classical Karman vortices in both their formation mechanism and dynamic behavior.

6. *Comparative Evaluation* Comparative analysis with established CFD techniques including the Finite Volume Method, QUICK scheme, and SIMPLE algorithm demonstrates that ROM-HPM provides competitive and often superior performance in terms of physically realistic solution, computational efficiency, and solution accuracy. By eliminating the need for outlet boundary conditions, ROM-HPM enables seamless extension to channels of arbitrary length and circumvents common numerical errors associated with traditional CFD. A systematic comparison across four methodological combinations: ROM-HPM (Continuous and Discrete) and CFD (Continuous and Discrete) further confirms that ROM-HPM, particularly in its continuous form, consistently outperforms CFD techniques, which suffer from discretization errors that hinder the proper transport of flow momentum. Therefore, proposed ROM-HPM is strong potential for addressing other highly nonlinear physical problems, particularly in micro-channels.
7. *Limitation and Future Scope:* OM-HPM/ROM-HPM scales well when increasing order of approximations, however, its performance deteriorates when non-essential unknowns are embedded with the linear operator. Future research will focus on extending ROM-HPM to address advanced unsteady and three-dimensional flow problems, as well as its application to various geometries and surface roughness. Further investigations will also consider alternative pressure-correction strategies, including the use of the Poisson equation. This expansion aims to further enhance the method's robustness and applicability in solving real-world fluid dynamics challenges.

Acknowledgement

Prof. Maiti would like to express his sincere gratitude to the Mathematical Research Impact Centric Support (ARG-MATRICS) under the Anusandhan National Research Foundation (ANRF) for financial support through Sanction Order No. ANRF/ARGM/2025/002126/MTR.

Authors' contributions

Tapas Roy have done mathematical calculation, developed the numerical code and partly written the manuscript. **Palash Mondal** conducted the CFD simulations, while **Dilip Kumar Maiti** conceived the problem, verified the results, and supervised the overall numerical computation and finalize the whole manuscript.

Funding

There is no individual funding available to conduct this work.

Data Availability

No datasets were generated or analysed during the current study.

Author ORCiD Information

Tapas Roy: 0000-0003-4530-0296, Dilip K. Maiti: 0000-0002-5226-0977

Declarations

Conflict of interests

The authors have no relevant financial or nonfinancial interests to disclose.

References

[1] Fefferman, C., Existence and smoothness of the Navier-Stokes equation, *4th ed.*, The Millennium Prize Problems, 2006.

[2] Versteeg, H. K., Malalasekera, W., An Introduction to Computational Fluid Dynamics: The Finite Volume Method, *2nd ed.*, Pearson Education, London, 2007.

[3] Abazari, R., Borhanifar, A., Numerical study of the solution of the Burgers and coupled Burgers equations by a differential transformation method, *Comput. Math. Appl.*, **59(8)**, 2711-2722 (2010). https://doi.org/10.1016/j.camwa.2010.01.039.

[4] Liao, S.J., Analytic solutions of the temperature distribution in Blasius viscous flow problems, *J. Fluid Mech.*, **453**, 411–425 (2002). https://doi.org/10.1017/S0022112001007169.

[5] Liao, S.J., On the analytic solution of magnetohydrodynamic flows of non-Newtonian fluids over a stretching sheet, *J. Fluid Mech.*, **488**, 189–212 (2003). https://doi.org/10.1017/S0022112003004865.

[6] Liao, S.J., Advances in the Homotopy Analysis Method, *World Scientific Publishing*, China (2014). https://doi.org/10.1142/8939.

[7] Liao, S.J., An Optimal Homotopy Analysis Approach for Strongly Nonlinear Differential Equations, *Commun. Nonlinear Sci. Numer. Simul.*, **15**, 2003–2016 (2010). https://doi.org/10.1016/j.cnsns.2009.09.002.

[8] Xu, H., Lin, Z.L., Liao, S.J., Wu, J.Z. & Majdalani, J., Homotopy based solutions of the Navier–Stokes equations for a porous channel with orthogonally moving walls, *Phys. Fluids*, **22**, 053601 (2010). https://doi.org/10.1063/1.3392770.

[9] Jiang, Y., Wang, F., A novel semi-analytical meshless method for Navier–Stokes equations arising in fractured rock masses, *Chin. J. Phys.*, **95**, 1069–1077 (2025). https://doi.org/10.1016/j.cjph.2025.03.007.

[10] Kimura, R., Numerical weather prediction, *J. Wind Eng. Ind. Aerodyn.*, **90**, 1403–1414 (2002). https://doi.org/10.1016/S0167-6105(02)00261-1.

[11] Suss, A., Mary, I., Le Garrec, T., Marié, S., A hybrid lattice Boltzmann–Navier–Stokes method for unsteady aerodynamic and aeroacoustic computations, *J. Comput. Phys.*, **485**, 112098 (2023). https://doi.org/10.1016/j.jcp.2023.112098.

[12] Beiser, F., Holm, H.H., Lye, K.O., Eidsvik, J., Multi-level data assimilation for ocean forecasting using the shallow-water equations, *J. Comput. Phys.*, **524**, 113722 (2025). https://doi.org/10.1016/j.jcp.2025.113722.

[13] White, F.M., Viscous Fluid Flow, *3rd ed.*, McGraw-Hill, Boston (2011).

[14] Majee, S., Maiti, S., Shit, G.C., Maiti, D.K., Spatio-temporal evolution of magnetohydrodynamic blood flow and heat dynamics through a porous medium in a wavy-walled artery, *Comput. Biol. Med.*, **135**, 104595 (2021). https://doi.org/10.1016/j.compbiomed.2021.104595.

[15] Panton, R.L., Incompressible Flow, *4th ed.*, Wiley, Hoboken, NJ (2013).

[16] Mondal, P., Maiti, D.K., Variable injection–suction and temperature on Couette–Poiseuille non-Newtonian flow through slippy microchannel: heat transfer and entropy generation, *J. Therm. Anal. Cal.*, **148**, 12225–12246 (2023). https://doi.org/10.1007/s10973-023-12539-w.

[17] Kundu, M., Vamsee, K., Maiti, D.K., Simulation and analysis of flow through microchannel, *Asia-Pac. J. Chem. Eng.*, **4**, 450–461 (2009). https://doi.org/10.1002/apj.232.

[18] Bhattacharyya, S., Maiti, D.K., Dhinakaran, S., Influence of buoyancy on vortex shedding and heat transfer from a square cylinder in proximity to a wall, *Numer. Heat Transf. A*, **50(6)**, 585–606 (2006). https://doi.org/10.1080/10407780600867761.

[19] Bhatt, R., Maiti, D.K., Alam, M.M., Zhou, Q., Flow around two square cylinders near a wall, *Phys. Fluids*, **37(3)**, 033621 (2025). https://doi.org/10.1063/5.0256028.

[20] Patankar, S.V., Numerical Heat Transfer and Fluid Flow, *1st ed.*, Hemisphere Publishing, New York, USA (1980).

[21] Feng, X., He, Y., Modified homotopy perturbation method for solving the Stokes equations, *Comput. Math. Appl.*, **61**, 2262–2266 (2011). https://doi.org/10.1016/j.camwa.2010.09.041.

[22] Saif, A.S.J.A., Analytical approximate solutions for two-dimensional incompressible Navier–Stokes equations, **49** (2015). https://api.core.ac.uk/oai/oai:ojs.localhost:article/26938.

[23] Waleffe, F., Homotopy of exact coherent structures in plane shear flows, *Phys. Fluids*, **15(6)**, 1517–1534 (2003). https://doi.org/10.1063/1.1566753.

[24] Liao, S.J., A uniformly valid analytic solution of two-dimensional viscous flow over a semi-infinite flat plate, *J. Fluid Mech.*, **385**, 101–128 (1999). https://doi.org/10.1017/S0022112099004292.

[25] Liao, S.J., Beyond Perturbation: Introduction to Homotopy Analysis Method, *1st ed.*, Chapman and Hall/CRC, New York (2003). https://doi.org/10.1201/9780203491164.

[26] Liao, S.J., Homotopy Analysis Method in Nonlinear Differential Equations, *1st ed.*, Springer Berlin, Heidelberg (2012). https://doi.org/10.1007/978-3-642-25132-0.

[27] Liu, Z., Liao, S.J., Steady-state resonance of multiple wave interactions in deep water, *J. Fluid Mech.*, **742**, 664–700 (2014). https://doi.org/10.1017/jfm.2014.2.

[28] Yang, X., Dias, F., Liao, S.J., On the steady-state resonant acoustic–gravity waves, *J. Fluid Mech.*, **849**, 111–135 (2018). https://doi.org/10.1017/jfm.2018.422.

[29] He, J.H., Homotopy perturbation technique, *Comput. Methods Appl. Mech. Eng.*, **178**, 257–262 (1999). https://doi.org/10.1016/S0045-7825(99)00018-3.

[30] Baxter, M., Gorder, R.A.V., Vajravelu, K., On the choice of auxiliary linear operator in the optimal homotopy analysis of the Cahn–Hilliard initial value problem, *Numer. Algor.*, **66**, 269–298 (2014). https://doi.org/10.1007/s11075-013-9733-8.

[31] Roy, T., Maiti, D.K., An optimal and modified homotopy perturbation method for strongly nonlinear differential equations, *Nonlinear Dyn.*, **111**, 15215–15231 (2023). https://doi.org/10.1007/s11071-023-08662-w.

[32] Roy, T., Maiti, D.K., General approach on the best fitted linear operator and basis function for homotopy methods and application to strongly nonlinear oscillators, *Math. Comput. Simul.*, **220**, 44–64 (2024). https://doi.org/10.1016/j.matcom.2024.01.004.

[33] Roy, T., Maiti, D.K., Refined variational iteration method through optimal linear operator and Lagrange multiplier: Local/global convergence, *Appl. Numer. Math.*, **212**, 1–28 (2025). https://doi.org/10.1016/j.apnum.2025.01.013.

[34] Roy, T., Maiti, D.K., Advances in Overcoming Methodological Limitations of HAM and HPM: OM-HPM (2025). https://doi.org/10.21203/rs.3.rs-8222560/v1.

[35] Roy, T., Soqi, A., Maiti, D.K., Wannan, R., Asad, J., Pendulum attached to a vibrating point: Semi-analytical solution by optimal and modified homotopy perturbation method, *Alex. Eng. J.*, **111**, 396–403 (2025). https://doi.org/10.1016/j.aej.2024.10.086.

[36] Roy, T., Maiti, D.K., Single/multi step optimal and modified homotopy perturbation method for strongly non-linear fractional initial value problems: Global series solution, *J. Comput. Sci.*, **94**, 102786 (2026). https://doi.org/10.1016/j.jocs.2026.102786.

[37] Liu, Y.Y., Liu, J.W., An attempt to apply the homotopy method to the domain of machine learning, *Expert Syst. Appl.*, **234**, 121098 (2023). https://doi.org/10.1016/j.eswa.2023.121098.

[38] Moghimi, M., Hejazi, F.S.A., Variational iteration method for solving generalized Burger–Fisher and Burger equations, *Chaos Solit. Fractals*, **33**, 1756–1761 (2007). https://doi.org/10.1016/j.chaos.2006.03.031.

[39] Kızıl, İ., Demirbilek, U., Çelik, E., Investigation of new analytical and numerical solutions of the extended (2+1)-dimensional Boussinesq equation using fractional derivative approaches, *J. Comput. Phys.*, **551**, 114654 (2026). https://doi.org/10.1016/j.jcp.2026.114654.

[40] Gorder, R.A., Vajravelu, K., On the selection of auxiliary functions, operators, and convergence control parameters in the application of the Homotopy Analysis Method to nonlinear differential equations: A general approach, *Commun. Nonlinear Sci. Numer. Simul.*, **14**, 4078–4089 (2009). https://doi.org/10.1016/j.cnsns.2009.03.008.

[41] Biazar, J., Ghazvini, H., Exact solutions for nonlinear Burgers' equation by homotopy perturbation method, *Numer. Methods Partial Differ. Equ.*, **25(4)**, 833–842 (2009). https://doi.org/10.1002/num.20376.

[42] Biazar, J., Aminikhah, H., Exact and numerical solutions for nonlinear Burger's equation by VIM, *Math. Comput. Model.*, **49**, 1394–1400 (2009). https://doi.org/10.1016/j.mcm.2008.12.006.

[43] Chen, Y., The Substitution Method, Createspace Independent Publishing Platform, United States (2017).

[44] Inc, M., On numerical solution of Burgers' equation by homotopy analysis method, *Phys. Lett. A*, **372**, 356–360 (2008). https://doi.org/10.1016/j.physleta.2007.07.057.

[45] Kolbig, K.S., The complete Bell polynomials for certain arguments in terms of Stirling numbers of the first kind, *Appl. Math. Comput.*, **51(1)**, 113–116 (1994). https://doi.org/10.1016/0377-0427(94)00010-7.

[46] Li, J., Liu, Z., Liao, S.J., Borthwick, A.G.L., Steady-state harmonic resonance of periodic interfacial waves with free-surface boundary conditions based on the homotopy analysis method, *J. Fluid Mech.*, **916**, A58 (2021). https://doi.org/10.1017/jfm.2021.253.

[47] Maiti, D.K., Dependence of flow characteristics of rectangular cylinders near a wall on the incident velocity, *Acta Mech.*, **222**, 273–286 (2011). https://doi.org/10.1007/s00707-011-0527-6.

[48] Maiti, D.K., Bhatt, R., Vortex shedding suppression and aerodynamic characteristics of square cylinder due to offsetting rectangular cylinder towards a plane, *Ocean Eng.*, **82**, 91–104 (2014). https://doi.org/10.1016/j.oceaneng.2014.02.033.

[49] Mondal, P., Maiti, D.K., Variable magnetization on hydrodynamic forward/backward/mixed power-law ferro-fluid flow through porous media microchannels: Entropy generation, *Int. J. Heat Fluid Flow*, **121**, 110439 (2026). https://doi.org/10.1016/j.ijheatfluidflow.2026.110439.

[50] Raisinghania, M.D., Ordinary and Partial Differential Equations, *18th ed.*, S. Chand Publishing, New Delhi (2016).

[51] Ramo, S., Whinnery, J.R., Van Duzer, T., Fields and Waves in Communication Electronics, *3rd ed.*, John Wiley & Sons, University of California, Berkeley (1994).

[52] Xu, D., Lin, Z., Liao, S.J., Stiassnie, M., On the steady-state fully resonant progressive waves in water of finite depth, *J. Fluid Mech.*, **710**, 379–418 (2012). https://doi.org/10.1017/jfm.2012.370.

[53] Yabushita, K., Yamashita, M., Tsuboi, K., An analytic solution of projective motion with the quadratic resistance law using homotopy analysis method, *J. Phys. A: Math. Theor.*, **40(29)**, 8403–8416 (2007). https://doi.org/10.1088/1751-8113/40/29/015.

[54] Zhu, H., Shu, H., Ding, M., Numerical solutions of two-dimensional Burgers' equations by discrete Adomian decomposition method, *Comput. Math. Appl.*, **60(3)**, 840–848 (2010). https://doi.org/10.1016/j.camwa.2010.05.031.

Supplementary Files

This is a list of supplementary files associated with this preprint. Click to download.

- Highlights.docx
- GraphicalAbstract3.pdf